Hexokinase regulates Mondo-mediated longevity via the PPP and organellar dynamics

Raymond Laboy[1,2], Marjana Ndoci[1], Maximilian Vonolfen[1,2], Eugen Ballhysa[1,2], Shamsh Tabrez Syed[1], Tim Droth[1], Klara Schilling[1,2], Anna Löhrke[1], Ilian Atanassov[1], Adam Antebi[1,2*]

1 Department of Molecular Genetics of Ageing, Max Planck Institute for Biology of Ageing, Cologne, Germany

2 Cologne Excellence Cluster on Cellular Stress Responses in Aging-Associated Diseases (CECAD), University of Cologne, Germany

*For correspondence: aantebi@age.mpg.de

Abstract

The transcriptional complex Mondo/Max-like, MML-1/MXL-2, acts as a convergent transcriptional regulatory output of multiple longevity pathways in *Caenorhabditis elegans*. These transcription factors coordinate nutrient sensing with carbohydrate and lipid metabolism across the evolutionary spectrum. While most studies have focused on the downstream outputs, little is known about the upstream inputs that regulate these transcription factors in a live organism. Here, we found that knockdown of various glucose metabolic enzymes decreases MML-1 localization in the nucleus and identified two hexokinase isozymes, *hxk-1* and *hxk-2,* as the most vigorous regulators of MML-1 function. Upon hexokinase knockdown, MML-1 redistributes to mitochondria and lipid droplets (LD) and concomitantly, transcriptional targets are downregulated and germline longevity is abolished. Further, we found that *hxk-1* regulates MML-1 through mitochondrial β-oxidation, while *hxk-2* regulates MML-1 by modulating the pentose phosphate pathway (PPP) and its coordinated association with lipid droplets. Similarly, inhibition of the PPP rescues mammalian MondoA nuclear translocation and transcriptional function upon starvation. These studies reveal how metabolic signals and organellar communication regulate a key convergent metabolic transcription factor to promote longevity.

Key words: MondoA/ChREBP, MML-1, lipid droplet, metabolism, aging, transcription

Introduction

Aging is a complex multifactorial process associated with organismal homeostasis demise and an increased risk of age-related diseases. One key aspect of aging is the dysregulation of gene expression and metabolism (Fischer et al., 2022). Many transcription factors that regulate metabolic pathways have been shown to control lifespan in the evolutionary spectrum (Clancy et al., 2001; Green et al., 2021; Lapierre et al., 2013; Selman et al., 2008; Wang et al., 2008). Changes in the activity of specific transcription factors have been shown to impact gene expression patterns and alter metabolic processes, leading to a decline in cellular function and an increased risk of age-related diseases (Benhamed et al., 2012; Carroll et al., 2015; Denechaud et al., 2008; Du & Zheng, 2021; Tong et al., 2009). Thus, understanding the interplay between metabolism and transcriptional regulation is crucial for gaining insight into the mechanisms underlying aging and developing novel strategies for promoting healthy aging and reducing the risk of age-related diseases.

MondoA and the Carbohydrate Response Element Binding Protein (ChREBP) are paralogue transcription factors that work in heterodimeric complexes with Max-like protein X (Mlx) and have been identified as key regulators of glucose metabolism and energy homeostasis. These transcription factors recognize and bind hexanucleotide tandem sequences (CANNTG) in the promoter regions called Enhancer box (E-box) sequences (Massari & Murre, 2000) of various genes involved in glucose uptake, utilization, and storage (Billin et al., 2000; Cha-Molstad et al., 2009; Sans et al., 2006; Stoltzman et al., 2008; Yamashita et al., 2001). In addition to their role in glucose metabolism, MondoA/ChREBP have also been shown to play a role in regulating lipid metabolism and cellular stress response (Iizuka et al., 2006; Ishii et al., 2004; Ma et al., 2006). Studies have suggested that changes in MondoA/ChREBP activity with age may contribute to age-related metabolic dysfunction, leading to a decline in glucose tolerance and increased risk of type 2 diabetes and obesity (Ghasemi et al., 2015; Iizuka et al., 2006; Richards et al., 2017; Yamamoto-Imoto et al., 2022).

In *Caenorhabditis elegans,* the transcriptional complex formed by MML-1 (MondoA/ChREBP homolog) and MXL-2 (Mlx homolog) is part of an integrated helix-loop-helix (HLH) network required for lifespan extension in diverse longevity pathways (Johnson et al., 2014; Nakamura et al., 2016). However, it is still unknown how these transcription factors integrate multiple upstream signals to regulate lifespan. In this work, we describe how metabolic inputs regulate MML-1 subcellular localization and function. We found that HXK-1 and HXK-2 regulate MML-1 cellular distribution and are required for germline longevity through the regulation of mitochondrial β-oxidation and the pentose phosphate pathway (PPP),

respectively. Moreover, inhibition of MML-1 nuclear translocation results in the relocalization of this transcription factor to mitochondria associated with lipid droplets (LD). This study provides key insights into how glucose and lipid metabolism directly impact transcriptional regulation and aging.

Results

Hexokinases are required for MML-1 subcellular localization and longevity

MondoA reportedly responds to glucose 6-phosphate (G6P) and other hexose phosphate sugars in cultured cells by translocating to the nucleus and regulating the expression of its downstream targets (Stoltzman et al., 2008, 2011). Nevertheless, little is known about the regulation of MondoA in an organism-wide setting, and most subsequent work has focused on the molecular mechanisms downstream of this transcription factor. Hence, we decided to investigate how MML-1 is regulated by upstream glucose metabolism in *C. elegans*. To address this, we performed a targeted RNA interference (RNAi)-based screen on genes encoding enzymes involved in glucose metabolism. Overall, we found a preponderance of decreased intestinal MML-1 nuclear localization when knocking down such genes (**Figure 1A-B, Supplementary Table S1**). Knockdown of most of the enzymes involved in glycolysis as well as the pyruvate dehydrogenase complex, which links glycolysis to the tricarboxylic acid (TCA) cycle via acetyl-CoA, decreased accumulation of nuclear MML-1 (**Supplementary Table S1**). Interestingly, whereas most enzymes in the TCA cycle also decreased nuclear MML-1, inhibition of the oxoglutarate dehydrogenase complex (OGDC) subunits *ogdh-1* and *dld-1* and the succinyl-CoA synthase (SCS) *suca-1* and *sucg-1* subunits increased MML-1 nuclear localization. We also observed that knockdown of enzymes involved in the oxidative and non-oxidative branches of the pentose phosphate pathway (PPP), phosphogluconate dehydrogenase (PGDH) *T25B9.9* and transketolase (TKT) *tkt-1* genes, respectively, triggered a strong increase in MML-1 nuclear accumulation (**Figure 1A-B**). Taken together, these data suggest that overall changes in glucose metabolism regulate MML-1 and that this transcription factor may sense the divergence of G6P to different branches of this network.

Our screen revealed that hexokinase knockdown had the most potent effect in decreasing MML-1 nuclear localization. This enzyme is involved in the first step of glucose metabolism, phosphorylating glucose to G6P, and is a critical mediator of cellular metabolism. Among the three *C. elegans* hexokinase genes, *hxk-1* and *hxk-2* more strongly affected MML-1 nuclear localization in two independent MML-1::GFP reporter strains (**Figure 1B, Supplementary Figure 1A**). To test whether the phosphotransferase activity of hexokinase is

102 responsible for regulating MML-1 nuclear localization, we used two drugs to inhibit
103 hexokinases pharmacologically. 3-Bromopyruvate (3-BrP) is an alkylating agent and HKII
104 inhibitor, and 2-deoxy-glucose (2-DG) is an analog of glucose phosphorylated to 2-DG6P
105 which cannot be further metabolized, thus inhibiting hexokinase function. Supplementation of
106 both drugs significantly decreased MML-1 nuclear localization compared to control
107 (**Supplementary Figure 1B-C**), indicating that hexokinase activity is driving MML-1 nuclear
108 translocation. We also tested the specificity of RNAi knockdown by using strains where the
109 three endogenous hexokinase loci were tagged with mKate2. We used these strains to evaluate
110 the protein levels by Western blot and found that each RNAi was specific to each isozyme
111 (**Supplementary Figure 1D-E**). As glycolysis is essential during development, we measured
112 the size (area and length) of worms fed with hexokinase RNAi egg-on. *hxk-1i* and *hxk-2i*
113 displayed no significant change in worm growth, while *hxk-3i* treated animals were somewhat
114 smaller (**Supplementary Figure 1F-G**). To determine if our observations were due to a change
115 in food intake, we counted pharyngeal pumping rate but found no significant difference
116 compared to the control (**Supplementary Figure 1H**), nor did we see an effect on worm
117 motility compared to control (**Supplementary Figure 1I**). Moreover, hexokinase knockdown
118 did not affect the steady-state levels of *mml-1* mRNA (**Supplementary Figure 1J**). Taken
119 together, these data indicate that there is no RNAi cross-reactivity among the hexokinase
120 isozymes and that the effects on MML-1 nuclear localization are not due to a decrease in food
121 consumption or developmental phenotype.
122 MML-1 works in a transcriptional complex with MXL-2, and previous studies have
123 demonstrated that MML-1 and MXL-2 are required for lifespan extension in multiple longevity
124 pathways, including germline-less *glp-1(e2141)* mutant (Nakamura et al., 2016). Hence, we
125 tested whether hexokinases influenced MML-1 subcellular localization in this longevity model.
126 As expected, MML-1 nuclear localization was increased in *glp-1(e2141)* as reported previously
127 (Nakamura et al., 2016), and upon *hxk-1* and *hxk-2* knockdown, MML-1 nuclear localization
128 was abolished in *glp-1(e2141)* mutants (**Figure 1C-D**). Changes in MML-1 nuclear
129 localization would be expected to modulate its transcriptional activity. To test this idea, we
130 next analyzed the expression of downstream targets reportedly linked to gonadal longevity
131 (Nakamura et al., 2016). We observed decreased expression of *mdl-1*, *lgg-2*, *swt-1*, and *fat-5*
132 under *hxk-1i* and *hxk-2i,* but not under *hxk-3i* (**Figure 1E, Supplementary Figure 1K**),
133 consistent with decreased MML-1 transcriptional activity. Since hexokinase knockdown
134 decreases MML-1 nuclear localization in the *glp-1(e2141)* longevity model, we reasoned that
135 the lifespan might also be abolished. Accordingly, *hxk-1i* and *hxk-2i* significantly decreased

136 *glp-1(e2141)* but did not affect wildtype lifespan (**Figure 1F**). Taken together, these data
137 indicate that hexokinases are upstream regulators of MML-1 nuclear localization and
138 transcriptional function in germline-mediated longevity.
139 Next, we tested whether the effect of hexokinase knockdown on MML-1 nuclear
140 localization and longevity was shared by other longevity pathways. On the one hand, we
141 observed that in *isp-1(qm150)* mutants, a model for mitochondrial longevity, *hxk-1* and *hxk-2*
142 knockdown decreased MML-1 nuclear localization and abolished lifespan extension (**Figure**
143 **1G-H**). On the other hand, while *mml-1* was required for the insulin signaling *daf-2(e1370)*
144 mutant longevity, *hxk-1* and *hxk-2* knockdown did not alter MML-1 nuclear localization nor
145 suppress the lifespan in this background (**Supplementary Figure 1L-M**). Further, we found
146 that MML-1 nuclear localization was increased in *raga-1(ok701)* mutants, a model for
147 mTORC1 longevity, and *mml-1* was required for lifespan extension (**Supplementary Figure**
148 **1N-O**). However, *hxk-1* and *hxk-2* knockdown did not suppress *raga-1(ok701)* longevity
149 (**Supplementary Figure 1P**). Collectively, these data suggest that while MML-1 acts as a
150 convergent factor in these four longevity pathways, it only requires HXK-1 and HXK-2 for
151 germline and mitochondrial longevity, but not for insulin and mTOR longevity.
152
153 *C. elegans hexokinases are differentially expressed*
154 Mammals harbor four hexokinases that differ in tissue expression, subcellular
155 localization, and affinity to glucose and G6P. However, knowledge of the nematode's isozymes
156 is limited. We used the hexokinase tagged with mKate2 strains to investigate the tissue-specific
157 expression and subcellular localization of the different isozymes by confocal microscopy. We
158 found that HXK-1 was expressed in the cytosol of neurons, pharynx, gonadal sheath, and
159 coelomocytes (**Figure 2A**). HXK-2 had a reticular expression pattern in neurons, muscle,
160 intestine, and hypodermis (**Figure 2B**). HXK-3 signal was diffused and highly expressed in
161 the pharynx, muscle, hypodermis, and intestine (**Supplementary Figure 2A**).
162 Human HKI and HKII have been shown to bind reversibly to the mitochondria (Sui &
163 Wilson, 1997). Binding depends on an intrinsic hydrophobic N-terminal sequence critical for
164 inserting into the outer mitochondrial membrane (Pastorino et al., 2002). Due to the reticular
165 expression pattern, HXK-2 was a plausible candidate to be mitochondrially localized. To
166 corroborate this idea, we crossed the HXK-2::mKate2 strain with a mitochondrial reporter that
167 expresses GFP with a mitochondrial targeting sequence under the body wall muscle promoter
168 *myo-3.* Indeed, we observed that full-length HXK-2 strongly co-localized with mitochondria
169 (**Figure 2C**). We also generated an HXK-2 mutant that lacks the first ten amino acids after the

170 initiator methionine (d10 HXK-2) and found that mitochondrial localization was abolished
171 entirely (**Figure 2C**). In summary, we found that hexokinases are differentially expressed in
172 *C. elegans* and identified HXK-2 as the worm mitochondrial hexokinase.
173
174 *Hexokinase knockdown increases MML-1 mitochondrial localization*
175 Since we observed that *mml-1* mRNA levels were unaffected by *hxk* knockdown and
176 saw a decrease in MML-1 nuclear localization upon hexokinase knockdown, we wondered
177 whether MML-1 might re-localize to another subcellular compartment. First, we crossed the
178 MML-1::GFP reporter strain with two compartmental markers and examined colocalization by
179 confocal microscopy. We looked at the lysosome/endosome reporter strain LMP-1::mKate2
180 but saw no evident colocalization in intestinal cells upon *hxk-2* knockdown or control
181 conditions (**Supplementary Figure 2B-C**). We had previously shown that MML-1 localizes
182 with mitochondria in the hypodermis (Nakamura et al., 2016); however, mitochondrial
183 subcellular localization in other tissues had not been examined. Hence, we crossed the
184 MML-1::GFP strain with the mitochondrial reporter TOMM-20::mCherry under the intestinal
185 promoter *ges-1p* and confirmed that MML-1 localized with mitochondria in the intestine
186 (**Figure 2D-E**). Under normal conditions, around 60-80% of the total MML-1 is nuclear, and
187 15% co-localizes with mitochondria. Interestingly, MML-1 mitochondrial localization was
188 increased to ~62% of total MML-1 upon *hxk-2i* (**Figure 2F**). Taken together, our data indicate
189 that upon *hxk-2* knockdown, MML-1 is excluded from the nucleus and re-localizes to a subset
190 population of mitochondria.
191
192 *Inhibition of mitochondrial β-oxidation rescues MML-1 nuclear localization under hxk-1i*
193 Many genes that regulate MML-1 localization are involved in mitochondrial
194 metabolism, such as OGDC and SCS, and inhibiting these complexes could activate stress
195 response pathways. Hence, we assessed whether MML-1 nuclear localization was associated
196 with the activation of mitochondrial stress response and oxidative stress. First, we observed
197 increased expression of *hsp-6::GFP*, a reporter for mitochondrial stress, upon knockdown of
198 mitochondrial components *ogdh-1*, *sucl-1*, and *sucl-2* as well as in control worms treated with
199 antimycin A (AA), a complex III inhibitor (**Supplementary Figure 2D**). However, inducing
200 mitochondrial stress with AA was not sufficient to affect MML-1 nuclear localization under
201 control conditions and *hxk-2* knockdown (**Supplementary Figure 2E**). Next, we wanted to
202 test whether an increase in oxidative stress affects MML-1 nuclear localization. We exposed

203 worms to the ROS-generating compound paraquat and observed induction of the oxidative
204 reporter *gst-4p::*GFP (**Supplementary Figure 2F**); however, we did not see any effect on
205 MML-1 nuclear localization at the concentrations tested (**Supplementary Figure 2G**). Taken
206 together, these data indicate that MML-1 regulation by glucose metabolism genes is
207 independent of mitochondrial and oxidative stress.

208 Hexokinase downregulation might be expected to cause a reduction in the reliance on
209 glycolysis and an increase in fatty acid metabolism as fuel for cellular maintenance (**Figure**
210 **2G**). Mitochondrial β-oxidation is an important pathway that generates acetyl-CoA for the
211 TCA cycle through the catabolism of fatty acids to produce reductants and energy. Hence, we
212 sought to investigate whether decreasing fatty acid oxidation could affect MML-1 nuclear
213 localization upon hexokinase knockdown. First, we measured the neutral lipid content by
214 feeding the worms with the labeled fatty acid C1-BODIPY-C12 and found increased total lipid
215 storage under hexokinase knockdown in the wildtype and *glp-1(e2141)* backgrounds
216 (**Supplementary Figure 2H**). Next, we measured the oxygen consumption rate (OCR) upon
217 hexokinase knockdown under basal conditions and with etomoxir supplementation, a
218 mitochondrial β-oxidation inhibitor that acts on the carnitine palmitoyltransferase (CPT).
219 Inhibition of the CPT decreases acyl-CoA import to mitochondria and changes in OCR are a
220 correlative measure of mitochondrial β-oxidation of fatty acids (Ramachandran et al., 2019).
221 We found no difference in basal OCR under *hxk-1*, *hxk-2*, and *mml-1* knockdown in the
222 wildtype background (**Figure 2H**). *glp-1(e2141)* animals showed decreased basal OCR
223 compared to wildtype, whereas *hxk-1* and *mml-1* knockdown significantly increased the basal
224 OCR compared to *glp-1(e2141)* (**Figure 2H**). Interestingly, we saw a greater percentage of
225 OCR reduction upon adding etomoxir under *hxk-1* knockdown in wildtype and under *hxk-1*,
226 *hxk-2*, and *mml-1* knockdown in *glp-1(e2141)* (**Figure 2I**), indicating higher mitochondrial
227 β-oxidation levels. We confirmed this result using the transcriptional reporter *acs-2p*::GFP, a
228 mitochondrial acyl-CoA synthase that is induced and required for fatty acid β-oxidation in *C.*
229 *elegans* (Van Gilst et al., 2005), and found increased expression upon *hxk-1* and *hxk-2*
230 knockdown (**Supplementary Figure 2I**).

231 We next wondered whether this increase in fatty acid oxidation was responsible for
232 decreased MML-1 nuclear localization under hexokinase knockdown. First, we performed a
233 double knockdown of *hxk-1* or *hxk-2* combined with *acs-2*. We found that MML-1 nuclear
234 localization was rescued upon *acs-2i* under *hxk-1* knockdown (**Figure 2J**). Interestingly, *acs-2i*
235 did not rescue MML-1 nuclear localization under *hxk-2* knockdown. We also

236 pharmacologically inhibited fatty acid oxidation by supplementing etomoxir and again saw the
237 rescue of MML-1 nuclear localization under *hxk-1* knockdown but no effect upon *hxk-2*
238 knockdown (**Figure 2K**). These data suggest that HXK-1 normally promotes MML-1 nuclear
239 localization by decreasing mitochondrial β-oxidation and reveal that the two hexokinases might
240 regulate MML-1 nuclear localization through somewhat independent pathways.
241
242 *hxk-2 regulates MML-1 function through increased PPP*
243 G6P can be diverted as a substrate for metabolic pathways other than glycolysis. Thus,
244 we wanted to test whether MML-1 could sense other branches of glucose metabolism. From
245 our RNAi screen, we observed increased MML-1 nuclear localization upon knockdown of two
246 enzymes from the PPP, *T25B9.9* and *tkt-1* (**Figure 1A-B**). The PPP is a cytosolic metabolic
247 pathway involved in the interconversion of 3 to 7-carbon sugars that generate precursors for
248 the biosynthesis of lipids, amino acids, and nucleotides (**Figure 3A**). It also maintains redox
249 homeostasis through NADPH production. To further address these findings, we tested the
250 effect of pharmacological inhibition PPP on MML-1 nuclear localization using
251 6-aminonicotinamide (6-AN), which is a competitive inhibitor of the G6P dehydrogenase
252 (G6DH) and phosphogluconate dehydrogenase (6PGD). These two enzymes generate NADPH
253 in the PPP. In agreement with our previous results, we observed increased MML-1 nuclear
254 localization after supplementation of 1 mM of 6-AN (**Figure 3B**). Moreover, we found that
255 *hxk-2i*, but not *hxk-1i*, significantly increased the NADPH levels (**Figure 3C**). Additionally,
256 we found that *hxk-2i* had increased TKT-1 enzymatic activity compared to the control (**Figure**
257 **3D**). These data suggest that inhibition of the mitochondrial hexokinase enhances the PPP.
258 Next, we sought to test the epistatic interaction of hexokinase and PPP knockdown on
259 MML-1 nuclear localization. For these experiments, we performed double RNAi of *hxk-1* and
260 *hxk-2* in combination with the 6PGD *T25B9.9* and transketolase *tkt-1*. Interestingly, knocking
261 down these enzymes rescued MML-1 nuclear localization under *hxk-2i* (**Figure 3E-F**) but did
262 not rescue the localization under *hxk-1i* (**Supplementary Figure 3A**). To evaluate MML-1
263 function, we measured its transcriptional readouts and found that knocking down the PPP under
264 *hxk-2i* rescued the expression of *lgg-2*, *mdl-1*, *swt-1*, and *fat-5* (**Figure 3G, Supplementary**
265 **Figure 3B-D**); however, it had no effect under *hxk-1i* (**Supplementary Figure 3E-H**).
266 Moreover, we observed lower levels of G6P upon double knockdown of hexokinases with
267 *T25B9.9* and *tkt-1* compared to control (**Figure 3H, Supplementary Figure 3I**). Taken
268 together, these data suggest that the PPP activity is increased upon knockdown of the

269 mitochondrial hexokinase HXK-2, and inhibiting the PPP is sufficient to rescue MML-1
270 function independent of G6P levels.
271 Finally, we asked whether reducing the PPP could impact *glp-1(e2141)* lifespan upon
272 *hxk-2* knockdown. Inhibition of the PPP has been reported to extend the lifespan in *C. elegans*
273 by activating the mitochondrial UPR^{mt} (Bennett et al., 2017). As reported previously, we found
274 a significant lifespan extension upon *tkt-1* knockdown in wildtype (**Figure 3I**). Moreover,
275 knockdown of the PPP in the *glp-1(e2141)* background had no additive effect on longevity,
276 suggesting that *glp-1* and *tkt-1i* may share common mechanisms in extending lifespan.
277 Consistent with our data, knockdown of *T25B9.9* and *tkt-1* rescued *glp-1(e2141)* longevity
278 upon *hxk-2i* (**Figure 3I, Supplementary Figure 3J**). Collectively, these data indicate that an
279 increase in the PPP under *hxk-2* knockdown suppresses MML-1 function, and reducing PPP
280 restores longer life, placing PPP epistatically downstream of *hxk-2*.
281
282 *MML-1 interactome uncovers potential regulators of its function and localization*
283 Given the mitochondrial localization of MML-1 and possibly other organelles, we
284 decided to identify potential MML-1 binding partners to better understand its subcellular
285 distribution. We used CRISPR/Cas9 to tag the endogenous MML-1 locus with a 3xFLAG tag.
286 MML-1::3xFLAG was immunoprecipitated from whole-worm lysates and potential interactors
287 were identified by mass spectrometry(**Supplementary Table S3**). We detected ca.1600 to
288 2000 different proteins from three biological replicates and observed that the biological
289 replicates clustered together (**Supplementary Figure 4A-B**). We detected several proteins in
290 the immunoprecipitation (IP), including MXL-2, an established MML-1 binding partner
291 (Pickett et al., 2007), and vitellogenins VIT-1, VIT-3, and VIT-4, which are highly abundant
292 yolk proteins (**Figure 4A**). Analysis of the top 50 co-enriched candidates in MML-1 IPs
293 revealed enrichment for nuclear and mitochondrial proteins (**Supplementary Figure 4C**). We
294 also found multiple enriched proteins from different organelles, including lipid droplets (LD).
295 Mitochondria and LD dynamically interact in highly active metabolic tissues, and it has
296 been shown that mitochondria associated with LD have specific metabolic behavior compared
297 to cytosolic mitochondria (*e.g.*, different dynamics, motility, and capacity to burn
298 carbohydrates and lipids) (Gordaliza-Alaguero et al., 2019; Rambold et al., 2015). LD are
299 organelles involved in multiple roles serving as nutrient reservoirs and participating in
300 signaling pathways, and their biogenesis or degradation is tightly coupled to carbohydrate
301 metabolism (**Figure 4B**). Interestingly, PLIN-1, one of the most abundant LD proteins, was
302 co-enriched in MML-1 IP (**Figure 4A**). Hence, we wanted to test whether MML-1 localized to

303 these organelles. First, we used LipiBlue, a dye to specifically visualize LD *in vivo* (Tatenaka
304 et al., 2019), and found that all LipiBlue stained structures were positive with the LD resident
305 proteins DHS-3::GFP and PLIN-1::mCherry (**Supplementary Figure 4D-F**), indicating that
306 this dye could be used as a reliable method for visualization of LD in *C. elegans*.
307 Next, we examined LipiBlue-stained animals co-expressing MML-1::GFP and
308 TOMM-20::mCherry and saw that MML-1 localized with LipiBlue-positive structures (**Figure**
309 **4C**). Interestingly, we observed that MML-1 appeared localized to mitochondria associated
310 with LD (**Figure 4C-D**). Moreover, this colocalization was significantly increased upon *hxk-2*
311 knockdown (**Figure 4E**). Inhibition of transaldolase and enzymes from the PPP have been
312 shown to activate a fasting-like response by increasing lipolysis and enhancing the breakdown
313 of LD (Bennett et al., 2017), including higher expression of the adipose triglyceride lipase
314 ATGL-1 (**Supplementary Figure 4G**). Therefore, we wondered whether the LD size
315 correlates with MML-1 nuclear localization. We knocked down *hxk-2* and *tkt-1* to decrease and
316 increase MML-1 nuclear localization, respectively. We observed a significant reduction in
317 diameter and the total amount of LDs upon knockdown of *tkt-1*, while *hxk-2i* did not have an
318 effect (**Figure 4F, Supplementary Figure 4H).** Double knockdown of *hxk-2* and *tkt-1*,
319 however, resulted in smaller and fewer LDs than the control. Collectively, these data suggest
320 that MML-1 can localize with a specific subpopulation of mitochondria associated with LD
321 and that inhibition of the PPP can rescue MML-1 nuclear localization upon *hxk-2i* correlated
322 with decreasing LD size.
323 To test whether LDs directly regulated MML-1 localization, we knocked down *dgat-2*
324 and *atgl-1*, two enzymes involved in LD metabolism. DGAT-2 is a diacylglycerol (DAG)
325 transferase that promotes LD droplet expansion, while ATGL-1 is a rate-limiting enzyme in
326 LD breakdown (**Figure 4B**). First, we measured the neutral lipid composition and found that
327 *atgl-1i* increased lipid levels while *dgat-2i* worms did not show significant changes under *ad*
328 *libitum* conditions (**Supplementary Figure 4I**). Next, we tested MML-1 nuclear localization
329 and observed that *dgat-2i* increased MML-1 nuclear localization while *atgl-1i* resulted in
330 decreased levels of nuclear MML-1 (**Figure 4G**). Finally, we did an epistatic analysis of LD
331 metabolism and the PPP and found that MML-1 nuclear localization in *atgl-1i* was rescued
332 upon *tkt-1* knockdown (**Figure 4H**), thus, suggesting that LD metabolism is upstream or
333 parallel to the PPP in MML-1 regulation.
334
335 *The PPP regulates MondoA function in mammalian cells*

336 We next asked whether the PPP regulation of MML-1 we observed in *C. elegans* was
337 conserved in mammals. Specifically, we wanted to determine whether inhibition of the PPP is
338 sufficient to induce MondoA translocation to the nucleus under contrasting conditions where
339 MondoA is mostly cytosolic (starvation media) or split between the nucleus and cytoplasm
340 (high-glucose growing media). To test this, we cultured the HEK293T cells in high-glucose
341 media with 6-AN and subsequently transferred the cells to either high-glucose media or
342 starvation media (**Supplementary Figure 5A**). First, we observed decreased NADPH/NADP+
343 ratio in cells treated with 6-AN and under starvation conditions (**Supplementary Figure 5B**).
344 Next, we found that in both conditions, MondoA nuclear localization was increased upon
345 inhibition of the PPP (**Figure 5A-B**), while there was no evident regulation of MondoA at the
346 transcript level (**Figure 5C**). Consistent with MondoA increased nuclear localization, we
347 observed increased expression of two of the best-described downstream targets of MondoA,
348 *TXNIP* and *ARRDC4* (**Figure 5D, Supplementary Figure 5C**). These findings indicate that
349 the PPP also regulates mammalian MondoA localization and transcriptional function.
350

351 **Discussion**

352 Nutrient sensing pathways and metabolism play a central role in modulating aging by
353 establishing metabolic states of resilience and survival. Although much work has focused on
354 identifying mediators of these processes, we still know little about how organisms coordinate
355 feedback loops of metabolic pathways and transcriptional responses to establish such states.
356 Here, we present novel mechanisms of carbohydrate and lipid metabolism regulating the
357 transcription factor MML-1/Mondo. We observed that MML-1 senses multiple steps of glucose
358 metabolism and found that hexokinases regulate MML-1 function through different
359 mechanisms in *C. elegans*. On the one hand, we found that under *hxk-2* knockdown, MML-1
360 re-localizes to mitochondria and LD, abolishing the longevity of germline-less worms and
361 mutants with reduced mitochondrial function. Moreover, we could rescue MML-1 function by
362 decreasing the PPP independent of the G6P levels. On the other hand, we found that *hxk-1*
363 knockdown decreased MML-1 function by upregulating mitochondrial β-oxidation. Thus, we
364 found two metabolic branches that converge on MML-1 to trigger a transcriptional response
365 and regulate longevity. We note that while MML-1 is required in four different longevity
366 models, namely *glp-1,isp-1, daf-2,* and *raga-1, hxk-1* and *hxk-2* were required only for *glp-1*
367 and *isp-1* mediated longevity. Presumably, the signal transduction wiring is different in *raga-1*
368 and *daf-2*, or their inputs into MML-1 work downstream or in parallel to the hexokinases.

369 MondoA and ChREBP transcription factors have well-established central roles in
370 glucose metabolism (Ma et al., 2006; Sans et al., 2006; Stoltzman et al., 2008; Yamashita et
371 al., 2001), but whether and how glucose metabolic circuits affect Mondo regulation in a whole
372 animal model is little explored. By performing a systematic RNAi-based targeted screen of
373 enzymes involved in glucose anabolism and catabolism, we found that MML-1 senses multiple
374 steps of glucose metabolism in the worm. Among the genes tested, we found MML-1 nuclear
375 localization to be broadly sensitive to the downregulation of glycolytic enzymes, and the
376 knockdown of hexokinase had the most profound effect. Hexokinase carries out the first step
377 in glucose metabolism, the phosphorylation of glucose to form G6P, which can be shunted to
378 multiple metabolic pathways, including glycolysis, the PPP, glycogenesis, and trehalose
379 production. Our findings are consistent with previous work in cultured cells showing that
380 MondoA localization is regulated by HKII, which is thought to stimulate nuclear localization
381 via the production of G6P (Sans et al., 2006). Additionally, MondoA senses other
382 phosphorylated hexoses, including allose and 3-*O*-methylglucose (Stoltzman et al., 2011).

383 Consistent with our genetic findings above, pharmacological inhibition of glycolysis
384 by supplementation with 3-BrP and 2-DG suppressed MML-1 nuclear localization. In contrast
385 to MML-1, MondoA has been shown to accumulate in the nucleus upon 2-DG in rat L6 cells
386 (Stoltzman et al., 2008). A possible explanation for this difference is that our treatment
387 represents a chronic exposure to 2-DG from development until adulthood, while the
388 experiments in cells may reflect an acute response. Overall, 2-DG has been used as a glycolytic
389 inhibitor because it can be phosphorylated by hexokinase to 2-DG 6-phosphate; however, it
390 cannot be further metabolized in glycolysis. Further evidence shows that 2-DG not only
391 functions as a catabolic inhibitor but can also be directed to the PPP or other pathways (Chi et
392 al., 1987; Ralser et al., 2008). Moreover, low concentrations of 2-DG have been shown to
393 extend lifespan by restricting glucose metabolism, while higher concentrations of 2-DG and
394 glucose shortened the lifespan in worms (Schulz et al., 2007, Lee et al., 2009), suggesting a
395 threshold for the benefits of glucose metabolism inhibition in lifespan.
396 Additionally, we found an important link between glycolysis and pyruvate metabolism
397 regulating MML-1 localization. Under aerobic conditions, pyruvate is imported to the
398 mitochondria and converted to acetyl-CoA to generate ATP and other reducing molecules. We
399 found that downregulation of the mitochondrial pyruvate carrier *mpc-1* and the pyruvate
400 dehydrogenase complex (**Supplementary Table S1**) also decreased MML-1 nuclear
401 localization and function. Further, we found MPC-1 enriched in the MML-1 interactome.

402 Interestingly, loss of *MPC1* in yeast has been shown to accumulate pyruvate, lower TCA cycle
403 intermediates, and reduce chronological aging (Bricker et al., 2012; Orlandi et al., 2014). *MPC1*
404 similarly regulates the disposition of glycolytic and TCA intermediates in flies and mammals
405 (Bricker et al., 2012). Pyruvate can also enter the TCA cycle through pyruvate carboxylase
406 PYC-1, which converts pyruvate to oxaloacetate. However, knockdown of *pyc-1* did not affect
407 MML-1 localization (**Supplementary Table S1**), suggesting that MML-1 may sense pyruvate
408 metabolism mainly through oxidative decarboxylation of acetyl-CoA.

409 We also found that MML-1 responds strongly to alterations in the TCA cycle. The TCA
410 cycle allows organisms to oxidize carbohydrates, fatty acids, and amino acids to provide energy
411 and intermediates for the biosynthesis of macromolecules. Interestingly, the knockdown of two
412 subunits of the OGDC, *ogdh-1* and *dld-1*, increased MML-1 nuclear localization. The OGDC
413 is a rate-limiting enzyme within the mitochondrial TCA cycle that decarboxylates
414 2-oxoglutarate to succinyl-CoA. It has been shown previously that supplementation of
415 2-oxoglutarate and knockdown of *ogdh-1* extends lifespan through inhibition of ATP synthase,
416 decreasing oxygen consumption, and increasing autophagy in an mTOR-dependent manner
417 (Chin et al., 2014). Whether MML-1 is required for this lifespan extension has yet to be
418 explored. Conceivably, the mitochondrial localization of MML-1 could help sense
419 2-oxoglutarate levels, and the accumulation of this metabolite could signal translocation to the
420 nucleus. Moreover, glutamine can be converted to glutamate and subsequently to
421 2-oxoglutarate during glutaminolysis and represents an important mechanism to replenish the
422 TCA cycle under different metabolic challenges. In this case, OGDC plays a pivotal role in
423 channeling anaplerotic reactions into the TCA cycle from glutamine and glutamate and other
424 amino acids that can ultimately be converted to 2-oxoglutarate (*i.e.*, histidine, proline, and
425 arginine) (Owen et al., 2002). Interestingly, increased glutamine-dependent anaplerosis has
426 been shown to regulate MondoA activity in BxPC-3 cells (Kaadige et al., 2009), though the
427 molecular mechanism remains unclear. Whether glutamine, glutamate supplementation, or
428 knockdown of glutamate dehydrogenase can regulate MML-1 nuclear localization remains to
429 be determined.

430 On the other hand, the TCA cycle can operate in reverse to restore TCA intermediate
431 levels (Dalziel & Londesborough, 1968). Increased levels of 2-oxoglutarate due to inhibition
432 of OGDC, or glutamine anaplerosis, can undergo reductive carboxylation by isocitrate
433 dehydrogenase to produce isocitrate. After that, aconitase can convert isocitrate to citrate,
434 which can be exported out of the mitochondria for *de novo* lipogenesis. MML-1 could help
435 orchestrate the metabolic rewiring of the TCA cycle with the fatty acid metabolism

436 transcriptional response. Notably, ChREBP has been shown to regulate many lipogenic
437 enzymes, including acetyl-CoA carboxylase (ACC), the fatty acid synthase (FAS), and
438 ATP-citrate lyase (ACLY) (Ishii et al., 2004; Postic et al., 2007). Accordingly, the MML-1
439 transcriptome shows clear regulation of several fatty acid metabolic enzymes (Nakamura et al.,
440 2016).

441 We observed that PPP pathway enzymes strongly influenced MML-1 nuclear
442 localization and function. The PPP is a cytosolic pathway involved in the interconversion of
443 sugars to generate precursors for the biosynthesis of lipids, amino acids, and nucleotides and
444 maintain redox homeostasis. We found that knockdown of PPP components, PGDH *T25B9.9*
445 and transketolase *tkt-1*, enhanced MML-1 nuclear localization, increased the transcription of
446 MML-1 target genes, and restored longevity to *glp-1(e2141)* animals under *hxk-2i*. The PPP is
447 the primary source of NADPH, which plays a vital role in many cellular processes, including
448 fatty acid, nucleotide, neurotransmitter, and cholesterol metabolism, and works as an essential
449 reducing agent (Ju et al., 2020). We found that pharmacological inhibition with 6-AN of the
450 two enzymes producing NADPH in the PPP increased MML-1 nuclear localization. We also
451 found increased levels of NADPH and lower levels of G6P under *hxk-2* knockdown.
452 Importantly, these observations suggest that residual G6P may be diverted to the PPP under
453 low mitochondrial hexokinase and further imply that metabolites other than G6P could regulate
454 MML-1 nuclear localization. What this other metabolite could be remains elusive, but a
455 simplifying notion is that MML-1 nuclear localization is promoted by intermediates in the
456 glycolysis or the PPP. Blocking entry into the PPP or TCA might be expected to accumulate
457 such metabolites and promote Mondo nuclear localization. Conversely, depletion of these
458 metabolites would disrupt Mondo nuclear localization and activity.

459 Another possibility is that Mondo organellar distribution is regulated at another scale.
460 Notably, a major output of the PPP and NADPH metabolism is the production of lipids.
461 Interestingly, we found that under *tkt-1* knockdown, fat levels decreased, and LDs were smaller
462 in diameter, suggesting that a reduction in LDs could signal MML-1 to translocate to the
463 nucleus. Consistently, transaldolase *tald-1* knockdown has been shown to increase lifespan and
464 decrease intestinal fat levels in the worm through increased activity of adipose triglyceride
465 lipase ATGL-1 (Bennett et al., 2017). This enzyme is involved in the metabolism of LD under
466 starvation to mobilize stored fats for energy production (Lee et al., 2014).

467 Interestingly, we found that although both HXK-1 and HXK-2 positively regulate
468 MML-1 function, they do so through different mechanisms **(Figure 5E)**. We observed that
469 inhibiting mitochondrial fatty acid β-oxidation is sufficient to rescue MML-1 nuclear

470 localization under *hxk-1* knockdown, but not *hxk-2* knockdown. Conversely, decreasing the
471 PPP rescued MML-1 localization under *hxk-2* knockdown independent of the G6P levels, but
472 not *hxk-1* knockdown. How both hexokinases activate different metabolic pathways to regulate
473 MML-1 remains unknown and could work at multiple levels.

474 First, there is evidence that differences in the subcellular location of hexokinases may
475 result in the compartmentalization of glucose metabolism, with the channeling of G6P to
476 different pathways (John et al., 2011; Wilson, 2003). Mitochondrial hexokinase has preferential
477 access to ATP generated in the mitochondria and provides efficient glycolysis coupling with
478 further pyruvate oxidation by the TCA cycle and oxidative phosphorylation (OXPHOS).
479 Furthermore, mammalian HKI and HKII have a dynamic localization, shuttling between the
480 mitochondrial outer membrane and the cytoplasm (John et al., 2011). Both mammalian
481 hexokinases have been reported to reversibly bind to mitochondria through their N-terminal
482 sequence (Roberts et al., 2014) and via their interaction with VDAC1 (Lindén et al., 1982).
483 This dual localization allows the cell to adapt to different metabolic requirements and maintain
484 energetic balance. Under high levels of G6P, HKII shuttles from the mitochondria to the
485 cytoplasm, causing cells to use glycogen as an energy source (John et al., 2011). The
486 subcellular localization also plays other significant roles in different signaling pathways. For
487 example, mitochondria-bound hexokinase has anti-apoptotic effects (Gottlob et al., 2001), and
488 increased N-acetylglucosamine upon pathogen exposure releases hexokinase from the
489 mitochondria and activates innate immune responses (Wolf et al., 2016). Here we found that
490 *C. elegans* HXK-2 is associated with mitochondria and that this localization is abolished by
491 deleting the first ten amino acids. However, we saw no effect upon *vdac-1* knockdown nor
492 dynamic localization of HXK-2 between mitochondria and cytosol (data not shown). Taken
493 together, these observations suggest that the nematode has dedicated mitochondrial (HXK-2)
494 and cytosolic (HXK-1 and HXK-3) hexokinases.

495 We also found differences in the tissue expression of the different hexokinase isozymes
496 of the nematode: HXK-1 was mainly found in the pharynx, neurons, gonadal sheath, and
497 coelomocytes, while HXK-2 was present in the hypodermis, body wall muscle, and intestine.
498 Consistently, RNAseq data from different tissues in *C. elegans* shows that *hxk-2* is the main
499 isozyme in the body wall muscle and intestine (Hutter & Suh, 2016). At the same time, *hxk-1*
500 is the main one expressed in pharyngeal muscle and neurons. This differential distribution
501 could explain how *hxk-1* and *hxk-2* differentially regulate MML-1 through β-oxidation and
502 PPP pathways. Notably, we scored MML-1 nuclear localization in the intestine in our

503 experiments, where *hxk-2* but not *hxk-1* is expressed. In the future, it will be important to see
504 whether *hxk-1* cell autonomously impacts *mml-1* nuclear localization within the same tissue,
505 such as the pharynx.

506 In any case, our observation that HXK-1 affects intestinal MML-1 nuclear localization
507 suggests cell non-autonomous signaling. What might be the nature of such cell non-
508 autonomous signaling? One possibility is the sterol hormone signaling pathway, which acts in
509 somatic reproductive tissue to regulate *glp-1(e2141)* longevity. Decreasing the activity of the
510 nuclear hormone receptor DAF-12, or its ligands dafachronic acids, abolishes the longevity of
511 germline-less worms (Gerisch et al., 2001; Yamawaki et al., 2010). Interestingly, carbohydrate
512 metabolism directly impacts the production of dafachronic acids as NADPH is required for the
513 last step of dafachronic acid biosynthesis by DAF-9 (Motola et al., 2006; Penkov et al., 2015).
514 Furthermore, DAF-9 is expressed in the somatic gonad (spermatheca) and XXX neurons in
515 adult animals (Gerisch & Antebi, 2004). Conceivably, hexokinase downregulation could affect
516 the production of NADPH and dafachronic acids regulating DAF-12 activity, thereby affecting
517 MML-1 function. It will be interesting to see whether dafachronic acid supplementation can
518 rescue MML-1 nuclear localization upon *hxk-1i* or *hxk-2i*.

519 The nervous system also plays a crucial role in integrating metabolic status and
520 systemic responses in a cell non-autonomous manner (Mutlu et al., 2020; Zhang et al., 2019).
521 Inhibition of the mTOR signaling pathway has been shown to extend lifespan across the
522 evolutionary spectrum (Kennedy & Lamming, 2016), and recent work has shown that restoring
523 *raga-1/*RagA or *rsks-1/*S6K in the nervous system is enough to entirely suppress the lifespan
524 extension conferred by mutation of these mTOR signaling factors (Zhang et al., 2019). In cells,
525 HKII has been shown to shuttle from the mitochondria and directly interact with mTOR under
526 glucose deprivation and inhibit its function resulting in an induction of autophagy (Roberts et
527 al., 2014). This interaction is dependent on the mTOR signaling (TOS) motif present in HKII
528 required for binding to Raptor. Interestingly, this TOS motif (KDIDI) is conserved in the
529 nematode HXK-1; however, HXK-2 and HXK-3 lack this sequence. Our finding that *raga-1*
530 mutants are epistatic to hexokinase knockdown for life span extension is consistent with a role
531 of mTOR signaling downstream of hexokinase. It would be interesting to study whether the
532 interaction between hexokinase and mTOR is conserved in *C. elegans* and whether decreasing
533 the main neuronal hexokinase (HXK-1) would result in mTOR-dependent inhibition of MML-
534 1.

535 Proteins tend to co-localize near their substrates to maximize specificity and regulate
536 signaling pathways. In particular, MondoA was first reported to be associated with the

537 mitochondria outer membrane in primary human SkMC cells through protein-protein
538 interaction (Sans et al., 2006). We have previously shown that this localization is conserved in
539 *C. elegans* (Nakamura et al., 2016). Mitochondria-bound MondoA has been proposed to have
540 preferential access to newly synthesized G6P from HKII to coordinate metabolism and
541 transcriptional response (Wilde et al., 2019). However, the identity of the mitochondrial factor
542 tethering MondoA at the mitochondria remains unknown.

543 Interestingly, our proteomics analysis of MML-1 immunoprecipitation showed
544 enrichment with proteins from different cellular compartments, including mitochondria, ER,
545 LD, and nucleolus, suggesting an important role of Mondo in integrating diverse organellar
546 signals. Localization to mitochondria was particularly conspicuous. Multiple nuclear
547 transcription factors are localized in the mitochondria, although dissecting their nuclear and
548 mitochondrial function is challenging (Leigh-Brown et al., 2010). On the one hand, nuclear
549 transcription factors have been shown to directly bind the mitochondrial genome to regulate
550 transcription, such as the cAMP response element-binding (CREB) protein (Marinov et al.,
551 2014). Interestingly, *mml-1(ok849)* loss-of-function mutants showed a decrease in all 12
552 mitochondrial-encoded genes compared to wildtype (Nakamura et al., 2016). However, this
553 could be indirect by regulating the mitochondrial transcription factor TFAM or mitochondrial
554 biogenesis (Li et al., 2005). On the other hand, transcription factors like p53 have been shown
555 to translocate to the mitochondrial outer membrane under apoptotic signals to interact with
556 Bcl-2 and promote membrane permeabilization and apoptosis (Marchenko et al., 2007). Future
557 studies will help elucidate whether MML-1/MondoA mitochondrial localization regulates
558 other cellular processes independent of its nuclear transcription function.

559 LD represents the main lipid storage in cells to balance metabolism and energy
560 demands. These organelles are essential for many signaling pathways and are required for
561 survival during fasting by mobilizing lipids for energy production. In *C. elegans,* LDs are
562 mainly localized in the intestine and hypodermis and are composed almost exclusively of TAG
563 (Vrablik et al., 2015). We found PLIN-1, one of the most abundant LD proteins, enriched in
564 the MML-1 interactome. Interestingly, we found that MML-1 colocalizes with LD *in vivo* in
565 the intestine. MondoA was previously seen in large-scale proteomics associated with LD
566 (Krahmer et al., 2018). It was shown that MondoA and Mlx localized with LD through
567 amphipathic helices in the C-terminus in SUM159 cells (Mejhert et al., 2020). The researchers
568 proposed a model in which MondoA/Mlx colocalization with LD inhibits its transcriptional
569 activity limiting glucose-dependent transcription. Work by Brunet and colleagues suggest that
570 MUFA intercalation into LD and peroxisomes somehow promotes longevity, though

571 downstream transcription factors are little explored (Papsdorf et al., 2023). Mitochondria and
572 LD physically interact with one another to regulate metabolism (Boutant et al., 2017). As
573 MondoA has also been shown to localize with mitochondria, it would be interesting to
574 understand the role of this organelle in regulating MondoA's association with LD. Although
575 the proteins involved in these contact sites are just beginning to be uncovered, both
576 PLIN1/PLIN-1 and ACSL1/ACS-13 have been proposed to tether mitochondria and LD
577 (Gordaliza-Alaguero et al., 2019).

578 Mitochondria bound to LD facilitate the coordination of TAG metabolism and fatty
579 acid oxidation. For example, lipases (*e.g.*, ATGL) in the LDs break down TAG to release free
580 fatty acids that can be activated in the mitochondria outer membrane by ACSL1 to fatty
581 acyl-CoA. This acyl-CoA can be imported into the mitochondria for β-oxidation. We propose
582 a model **(Figure 5E)** in which MML-1 interacts with specific mitochondria associated with LD
583 to orchestrate a transcriptional response depending on fuel utilization. Under normal
584 conditions, glucose stimulates MML-1 translocation to the nucleus to activate the transcription
585 of glycolytic enzymes. In contrast, upon blockage of glycolysis (*e.g.,* hexokinase knockdown),
586 the cell utilizes fatty acids to produce ATP, re-localizing and inhibiting MML-1 at the
587 mitochondria associated with LD.

588

589 **Materials and Methods**

590 *Worm growth and RNAi treatment*

591 *C. elegans* worm strains were grown and maintained on nematode growth medium
592 (NGM) plates seeded with *E. coli* OP50 strain as the primary food source. Worms were grown
593 at 20 °C unless stated otherwise. *glp-1(e2141)* strains were maintained at 15 °C. All worm
594 strains are listed in **Supplementary Table S4**. Worms were synchronized by 4 to 6 h egg lays
595 at 20 °C. For experiments including *glp-1(e2141)*, egg lays were performed at 15 °C, and the
596 eggs were upshifted to 25 °C for 52 to 56 h to induce the germline-less phenotype. After *glp-1*
597 induction, worms were downshifted to 20 °C until the day of analysis or collection.

598 The NGM media for RNAi knockdown was supplemented with 1 mM isopropyl
599 β-1-D-thiogalactopyranoside (IPTG) and 100 μg mL^{-1} ampicillin. The plates were seeded with
600 the RNAi-expressing *E. coli* HT115 (DE3) strain transformed with the L4440 vector from the
601 Ahringer and Vidal libraries (Kamath & Ahringer, 2003; Rual et al., 2004), or cloned for this
602 work. Bacteria containing luciferase RNAi cloned into the L4440 vector were used as controls.
603 Worms were grown on RNAi plates egg-on in all the experiments.

604

605 *Cell culture experiments*

606 HEK293T cells were maintained in DMEM medium 4.5 g/L D-glucose (Gibco)
607 supplemented with 10% FBS (Gibco). For blocking the PPP, cells were supplemented with 16
608 and 100 μM 6-AN for 24 to 48 h. After, cells were washed and added fresh DMEM medium
609 or transferred to starvation media (NaCl 140 mM, $CaCl_2$ 1 mM, $MgCl_2$ 1 mM, HEPES pH 7.4
610 20 mM, BSA 1%) for 6 h. Cells were collected for immunofluorescence, RNA extraction, and
611 metabolite quantification.

612 For addressing MondoA localization, cells were fixed with 4% paraformaldehyde (PFA) for
613 15 min at room temperature. Following fixation, the samples were washed 3 times with 500
614 μL DPBS, followed by 500 μL of methanol 99% for 5 min at -20 °C, and washed twice with
615 500 μL of DPBS and three times with TBST 1X. Cells were blocked with 10% goat serum
616 diluted in DPBS for 1 h at room temperature. Cells were incubated with 200 μL of the Anti-
617 MondoA antibody (Bethyl Laboratories, A303-195A) 1:500 diluted in goat serum overnight at
618 4 °C. Next, cells were washed 3 times with DPBS containing Triton x-100 (PBST) and similarly
619 incubated with 200 μL of Alexa-488 secondary antibody (Invitrogen, A21206) 1:500 diluted
620 in the goat serum at room temperature and covered in aluminum foil for 2 h. After washing 3
621 times with 500 μL of PBST, the samples were covered with a mounting medium containing
622 DAPI. The cells were cured for 24 h at room temperature in the dark and then stored at 4 °C.

623

624 *Demographic analysis*

625 Lifespan analyses were conducted by synchronizing worms by egg lay. All animals
626 were kept at 20 °C egg on, or transferred to 20 °C on day one of adulthood for the experiments
627 including *glp-1(e2141)*. More than 120 worms were used per strain/condition with 20-30
628 worms per 6 cm plate. Worms were transferred every other day to fresh plates until they
629 stopped laying eggs and scored every time they were transferred. Animals with internal
630 hatching and vulva protrusions were censored from the analysis. All lifespans were performed
631 by blinding the genotypes/RNAi. Demographic parameters like mean, median, and maximum
632 lifespan were calculated and plotted using GraphPad Prism 9 software.

633

634 *Oxygen consumption rate measurements*

635 Oxygen consumption rates (OCR) measurements in *C. elegans* were based on
636 (Koopman et al., 2016). Worms were synchronized by egg lay. 10 to 15 adult worms were

637 transferred to a Seahorse XF96 Cell Culture Microplate (Agilent) with 200 μL of M9 buffer.
638 OCR was measured using the Seahorse XFe96 Analyzer (Agilent). To measure mitochondrial
639 fatty acid β-oxidation, basal oxygen consumption was measured followed by injection of
640 etomoxir (final well concentration 500 μM) and finally injection of sodium azide (final well
641 concentration 40 mM), all measured five times. OCR was normalized to the number of worms
642 with at least six technical replicates.
643
644 *Body measurements, pharyngeal pumping rates, and motility assay*
645 Worms were imaged or recorded using the Leica stereo microscope MDG41 equipped
646 with Leica DFC3000G monochrome camera with a 6.3X magnification. For measuring the
647 body length and area, >20 worms were transferred to a drop of sodium azide 50 mM, imaged,
648 and analyzed in Fiji imaging software. To measure the pharyngeal pumping rates, worms were
649 transferred to a new plate, acclimated on the plates without a lid for 10 min, and then recorded
650 for 30 s. Worm motility was assessed by placing >20 worms in a drop of M9 buffer and
651 recorded for 30 s using the Leica M80 Binocular Microscope equipped with the Leica MC170
652 HD camera. Videos were analyzed to count the thrashing of each worm.
653
654 *Molecular cloning*
655 Plasmids were constructed by classical cloning or Gibson Assembly. Restriction
656 enzymes from NEB were used according to the manufacturer's instructions. Custom primers
657 were designed with SnapGene v.5.3.2 and NEBuilder Assembly Tool v.2.5.4 (**Supplementary**
658 **Table S5**). For classical cloning, digested plasmids and amplicons were ligated using the T4
659 DNA Ligase according to the manufacturer's instructions (New England Biolabs). For Gibson
660 Assembly, digested plasmid and amplicon were assembled using NEBuilder HiFi DNA
661 Assembly Master Mix (New England Biolabs) according to the manufacturer's instructions.
662 Plasmids were transformed into *E. coli* DH5α (Life Technologies) strain using the heat shock
663 protocol and plated on LB media supplemented with ampicillin.
664
665 *RNA extraction and RT-qPCR*
666 Worms were synchronized by egg lay for 4 h and collected once they reached the young
667 adult stage in 15 mL conical tubes. The worm pellet was subjected to 4 cycles of freeze and
668 thaw with liquid nitrogen and a water bath at ~37 °C. To lyse the worms, 200 μL of 1.0 mm
669 Zirconia/Silica beads (FisherScientific) were added and transferred to the TissueLyser LT

670 (Qiagen) for 30 min, full speed at 4 °C. Samples were incubated for 5 min at RT. After, 200
671 μL chloroform was added and centrifuged at 12,000 g for 15 min at 4 °C. The top aqueous
672 phase was transferred to a new 1.5 mL tube and mixed with 200 μL of ethanol. The RNA
673 purification was performed using the RNeasy Mini Kit (Qiagen) according to the
674 manufacturer's instructions. The concentration and purity of the RNA samples were quantified
675 using the NanoPhotometer NP80 spectrophotometer (Implen).
676 cDNA was prepared after extracting total RNA from young adult worms or cell extracts
677 using the iScript cDNA Synthesis Kit (BioRad) according to the manufacturer's instructions.
678 Primers, cDNA, and Power SYBR Green Master Mix (Applied Biosystems) were transferred
679 to a 384-well plate using the JANUS automated workstation (PerkinElmer) with four technical
680 replicates per genotype/gene. The reaction was quantified using the ViiA 7 Real-Time PCR
681 system machine (Applied Biosystems). *cdc-42* was used as an endogenous control for the
682 quantification. The complete primer sequences are in **Supplementary Table S5**.
683
684 *Oxidative stress assay*
685 Worms were grown on NGM plates until day 1 adults and then transferred to NGM
686 supplemented with paraquat at 15 and 35 mM for 6 h. As control, we used the CL2166 strain
687 that contains the transcriptional reporter *gst-4p*::GFP. MML-1::GFP nuclear localization was
688 measured in the intestine.
689
690 *Protein extraction and Western blot analysis*
691 Worms were harvested from a mixed population or synchronized by egg lay or
692 bleaching with M9 buffer and washed three times. The worm pellet was snap-frozen in liquid
693 nitrogen and stored at -80 °C until extraction. The pellet was resuspended in liquid lysis buffer
694 supplemented with cOmplete ULTRA EDTA-free protease inhibitors (Roche) and PhosSTOP
695 phosphatase inhibitors (Roche) and sonicated with Bioruptor Plus (Diagenode S.A.) coupled
696 to Minichiller 300 (Huber) for 15 cycles of 30 sec sonication, 30 sec rest at 4 °C. The total
697 protein extract was cleared by spinning down at 20,817 g for 10 min at 4 °C. Supernatant was
698 transferred to a new tube, and protein was quantified using Pierce BCA Protein Assay Kit
699 (ThermoFisher Scientific) according to the manufacturer's instructions. Equal amounts of
700 protein were mixed with 4X loading sample buffer containing DTT 50 mM and boiled at 95
701 °C for 10 min. Samples were loaded onto an SDS-PAGE PERCENTAGE gel (BioRad), and
702 proteins were then transferred onto a nitrocellulose membrane (BioRad) using the Trans-Blot

703 Turbo Transfer System (BioRad). Membranes were blocked for 1 h at RT with 5% milk in
704 TBST. Primary and secondary antibodies were diluted in 5% bovine serum albumin (BSA) in
705 TBST and incubated for 2-18 h at 4 °C. Antibodies: RFP Tag Polyclonal Antibody 1:1000
706 (ThermoFisher Scientific, R10367), Monoclonal ANTI-FLAG M2, Clone M2 1:1000 (Sigma
707 Aldrich, F1804), Anti-beta Actin Antibody 1:1000 (Abcam, Ab8224), Anti-rabbit IgG (H+L)
708 1:5000 (Invitrogen, G21234), Anti-mouse IgG 1:5000 (Invitrogen, G21040), Rabbit Anti-
709 Mouse IgG (Ligh Chain Specific) (D3V2A) mAB (HRP Conjugate) 1:5000 (CST, 58802). The
710 membranes were washed three times with TBST for 10 min at RT in-between incubation with
711 the antibodies and after the secondary. The signals were detected using Western Lightning
712 Plus-ECL, Enhanced Chemiluminescence Substrate (PerkinElmer), and imaged in the
713 ChemiDoc MP Imaging System with Image Lab software (BioRad).
714
715 *Immunoprecipitation*
716 Worms were collected from a mixed population from twenty 10 cm plates, transferred
717 into 15 mL conical tubes with M9 buffer, and washed three times. Worms were snap-frozen in
718 liquid nitrogen and stored at -80 °C until extraction. The worm pellet was resuspended in lysis
719 buffer supplemented with cOmplete ULTRA EDTA-free protease inhibitors (Roche) and
720 PhosSTOP phosphatase inhibitors (Roche). Worms were sonicated with Bioruptor Plus
721 (Diagenode S.A.) coupled to Minichiller 300 (Huber) for 30 cycles of 30 sec sonication, 30 sec
722 rest at 4 °C. The total extract was cleared by spinning down at 20,817 g for 15 min at 4 °C.
723 Supernatant was transferred to a new tube, and protein was quantified using Pierce BCA
724 Protein Assay Kit (ThermoFisher Scientific) according to the manufacturer's instructions.
725 The Anti-FLAG M2 magnetic beads (Sigma) were resuspended and equilibrated with
726 TBST buffer. A total of 7 mg of total protein extract in 800 µL was mixed with the magnetic
727 beads and incubated overnight at 4 °C. The next day, the supernatant was removed and stored
728 for WB analysis. The beads were washed 3 times with 1 mL of cold washing buffer #1
729 (Tris/HCl, pH 7.4 20 mM, NaCl 300 mM, EDTA 1 mM, NP-50 0.5%), and 3 times with 1 mL
730 of cold washing buffer #2 (Tris/HCl, pH 7.4 20 mM, NaCl 300 mM, EDTA 1 mM). In the last
731 wash, 500 µL of washing buffer #2 was added, and 100 µL were stored for WB analysis.
732 To elute samples for mass spectrometry, 100 µL of elution buffer (Trypsin 5 ng/µL,
733 Tris/HCl, pH 7.5 50 mM, Tris(2-carboxyethyl)phosphine (TCEP) 1 mM, Chloroacetamide
734 (CAA) 5 mM) were added and incubated 30 min at RT. The supernatant was transferred to a

735 new 0.5 mL tube and incubated overnight at 37 °C. The next day, formic acid was added to a
736 final concentration of 1% to stop the digestion. Peptides were stored at -20 °C until purification.
737 The peptides were cleaned and purified with StageTip. A 30 µg C18-SD tip was
738 hydrated with 200 µL of methanol, followed by 200 µL of 40% acetonitrile (ACN)/0.1% formic
739 acid (FA). 200 µL of 0.1% FA were added to equilibrate the C18-SD. The digested peptides
740 were dissolved in 0.1% FA and added to the C18-SD and washed once with 0.1% FA. To elute
741 the peptides, 80 µL of 40% ACN/0.1% FA was added, and elutes were collected in 0.5 µL
742 tubes and dried in centrifugal vacuum Concentrator Plus (Eppendorf) for 45 min at 45 °C.
743
744 *LC-MS/MS analysis*
745 Peptides were separated on a 25 cm, 75 µm internal diameter PicoFrit analytical column
746 (New Objective) packed with 1.9 µm ReproSil-Pur 120 C18-AQ media (Dr. Maisch) using an
747 EASY-nLC 1200 (ThermoFisher Scientific). The column was maintained at 50 °C. Buffer A
748 and B were 0.1% FA in water and 0.1% FA in 80% CAN, respectively. Peptides were separated
749 on a segmented gradient from 6 to 31% buffer B for 57 min and from 31 to 44% buffer B for
750 5 min at 250 nl/min. Eluting peptides were analyzed on an Orbitrap Fusion Tribrid mass
751 spectrometer (ThermoFisher Scientific). Peptide precursor m/z measurements were carried out
752 at 60,000 resolution in the 350 to 1,500 m/z range. The most intense precursors with charge
753 states from 2 to 7 were selected for HCD fragmentation using 27% normalized collision energy.
754 The cycle time was set to 1 sec. The m/z values of the peptide fragments were measured at a
755 resolution of 50,000 using an AGC target of 2e5 and 86 ms maximum injection time. Upon
756 fragmentation, precursors were put on a dynamic exclusion list for 45 sec.
757 The raw data were analyzed with MaxQuant v.1.6.1.0 (Cox & Mann, 2008). Peptide
758 fragmentation spectra were searched against the canonical and isoform sequences of the *C.*
759 *elegans* reference proteome (proteome ID UP000001940, downloaded December 2018 from
760 UniProt). Methionine oxidation and protein N-terminal acetylation were set as variable
761 modifications; cysteine carbamidomethylation was set as fixed modification. The digestion
762 parameters were set to "specific" and "Trypsin/P". The minimum number of peptides and razor
763 peptides for protein identification was 1; the minimum number of unique peptides was 0.
764 Protein identification was performed at a peptide spectrum match and protein false discovery
765 rate of 0.01. The "second peptide" option was on. Successful identification was transferred
766 between the different raw files using the "Match between runs" option. Label-free
767 quantification (LFQ) (Cox et al., 2014) was performed using an LFQ minimum ratio count of

768 2. LFQ intensities were filtered for at least two valid values in at least one group and imputed
769 from a normal distribution with a width of 0.3 and a downshift of 1.8. Differential expression
770 analysis was performed using *limma* package v.3.34.9 (Ritchie et al., 2015) in R v.3.4.3 (R
771 Core Team, 2017).
772
773 *G6P and $NADP^+$/NADPH measurements and TKT activity assay*
774 G6P and $NADP^+$/NADPH were measured from total worm extracts or cell extracts
775 using the Glucose-6-Phosphate Assay Kit (Sigma MAK014) and the NADP/NADPH-Glo
776 Assay (Promega G9081), respectively, following the manufacturer's instructions. The
777 Transketolase Activity Assay Kit (Fluorometric) (Sigma MAK420) was used to measure TKT
778 activity in worm extracts following the manufacturer's instructions. Samples were normalized
779 to total protein concentration.
780 *glp-1(e2141)* strains were used to avoid signals from the germline. Briefly, worms were
781 synchronized as mentioned previously, collected in a 15 mL conical tube, and washed three
782 times with M9 buffer. Worms were snap-frozen in liquid nitrogen and sonicated using the
783 Bioruptor Plus (Diagenode S.A.) coupled to Minichiller 300 (Huber) for 15 cycles of 30 sec
784 sonication, 30 sec rest at 4 °C. Worms' extracts were cleared by centrifugation at 20,817 g for
785 15 min at 4 °C. Samples were always kept on ice. As mentioned previously, part of the samples
786 was used to quantify protein, and the rest was used to quantify the metabolites.
787 For G6P colorimetric detection, samples were run in technical duplicates in a 96-well
788 plate. The standard curve was made using the G6P Standard solution provided by diluting with
789 ddH_2O to generate 0 (blank), 2, 4, 6, 8, and 10 nmol/well standards. Samples were combined
790 with the reaction mix in each well and mixed for 30 min at RT, protecting the plate from the
791 light. The absorbance was measured at 450 nm using the POLARstar OMEGA Plate Reader
792 with Luminescence (BGM Labtech). For the analysis, all samples were corrected for the
793 background. The standard curve was generated with the appropriate values obtained by the
794 standards mentioned previously, and the amount of G6P in each sample was calculated with
795 the standard curve. Values were normalized to protein levels.
796 For the $NADP^+$/NADPH bioluminescent assay, samples were run in technical
797 duplicates in a 96-well plate. 50 µL of worm lysis in M9 buffer were incubated with 50 µL
798 base solution with 1% DTAB. Samples were split into two: one to measure $NADP^+$ and the
799 other to measure NADPH. Samples were incubated with or without 25 µL 0.4 N of HCl to
800 measure $NADP^+$ or NADPH, respectively, at 60 °C for 15 min, and then the plate was

801 equilibrated for 10 min at RT. Next, 25 µL of Trizma base were added to each well of acid-
802 treated samples to neutralize the acid and 50 µL of HCl/Trizma solution to each well of base-
803 treated samples. An equal amount of the NADP/NADPH-Glo Detection Reagent was added to
804 each well and mixed at RT for 30 min by protecting the plate from the light. The luminescence
805 was recorded using the POLARstar OMEGA Plate Reader with Luminescence (BGM
806 Labtech). Samples were corrected to background luminescence. The relative luminescent units
807 were standardized to the protein concentration.
808
809 *Brightfield and fluorescent imaging*
810 Brightfield and fluorescent images with higher resolution were acquired using the Zeiss
811 Axio Imager Z1 Fluorescent Microscope equipped with the Digital Microscope Camera Axio
812 Cam Mono 506 and the IcC5 true color camera. For fluorescent microscopy, the microscope
813 used a Colibri 7 LED Light Source and the filters sets GFP (Set 38 HE), TR (Set 45), and TL.
814 The software used was Zeiss Zen v2.3.69.1017. Brightfield and fluorescent images were also
815 acquired with the Leica stereo microscope MDG41 equipped with Leica DFC3000G
816 monochrome camera. The microscope was equipped with the Leica EL6000 external light
817 source. The software used was the Leica Application Suite X v3.7.5.24914.
818 All dyes were added to the bacterial lawn, incubated egg on, and protected from the
819 light until the day of imaging. Final solutions were made by diluting in M9 buffer. LipiBlue
820 (Dojindo) was resuspended in 100 µL of DMSO to make a 100 µM stock. The final
821 concentration used was 1 µM. C1-BODIPY-C12 500/510 (ThermoFisher Scientific) was
822 dissolved in DMSO to make a 5 mM stock. The final concentration used was 1 µM. Worms
823 were mounted on a slide with a 5% agarose pad using sodium azide 50 mM. Levamisole 2 mM
824 was used as an anesthetic to image mitochondria.
825 Nuclear localization of MML-1::GFP was quantified in intestinal cells from day one
826 adult worms. Worms anesthetized with sodium azide 40 mM. At least, 20 worms were imaged
827 per genotype/condition. Quantification of the transcription factor nuclear localization was
828 performed by manually selecting each nucleus and calculating the pixel intensity per area. The
829 same area was used to calculate the cytosolic and background signal. Values were corrected by
830 background subtraction. Nuclear localization was calculated by dividing the nuclear signal
831 from the cytosolic signal.
832
833 *Confocal Imaging*

834 Confocal images were acquired with Leica TCS SP8 confocal microscope equipped
835 with a white light laser and a 63X 1.4 NA oil objective. The microscope was also equipped
836 with HyD detectors for fluorescent images and a PMT detector for the bright field. The LAS
837 X Life Science software was used to acquire images and 3D reconstruction. When multiple
838 fluorescent proteins or dyes were imaged, sequential scanning was used to reduce the bleed-
839 through of the signal from one channel to another. All images used for colocalization analysis
840 were deconvoluted with the installed LIGHTNING package to optimize the images and reduce
841 background noise.
842
843 *Statistical analysis and software*
844 The results are presented as mean + SD or SEM, as the figure legends indicate. The
845 number of biological replicates is shown in the figure legends as "N", while the number of
846 worms is presented as "n". Before comparing groups, the data were tested for Gaussian
847 distribution using the Kolmogorov-Smirnov normality test with Dallal-Wilkinson-Lilliefor *p*-
848 value. For normally distributed data, unpaired *t*-test with Welch's correction or one-way
849 ANOVA with Brown-Forsythe and Welch's corrections were calculated in GraphPad Prism 9
850 (GraphPad software). For lifespan analysis, *p*-values were calculated using Log-rank (Mantel-
851 Cox) test. Statistical data from all the lifespans are included in **Supplementary Table S2**.
852 Statistical significance for qPCR experiments was calculated with two-tailed *t*-test. For
853 colocalization analysis, Costes' randomization was performed to determine statistical
854 significance. Significance levels are ns = not significant $p>0.05$, * $p<0.05$, ** $p<0.01$, ***
855 $p<0.001$, **** $p<0.0001$.
856 Image analysis was performed using open-source Fiji package software. Additional
857 JACoP (Bolte & Cordelières, 2006) plugin was used for colocalization analysis. Densitometry
858 analyses were performed using GelAnalyzer v.19.1. Graphs were generated in GraphPad Prism
859 9 and using custom R scripts.
860
861 **Acknowledgments**
862 We would like to thank the CGC (University of Minnesota) and SunyBiotech for some
863 of the strains used in this study. We also thank Katrin Wollenweber and Nadine Hochhard for
864 their technical assistance and the Proteomics, Bioinformatics, and FACS & Imaging Core
865 Facilities at the MPI AGE for their support. Special thanks to Özlem Karalay, Andrea Annibal,
866 Roberto Ripa, Sarah Kreuz, and Victoria Martínez Miguel for the discussions and comments.

This work was funded by the Max Planck Society and the Cologne Graduate School for Ageing Research (CGA).

Authors contributions

A.A. and R.L. designed the experiments and wrote the manuscript. R.L. performed most of the experiments. M.N. established and performed the MondoA localization upon PPP inhibition in cell culture, M.V. acquired and processed the samples for proteomics and repeated biological replicates, E.B. measured the $NADPH/NADP^+$ levels in mammalian cells, I.A. performed proteomics.

Competing interests

The authors declare no competing interests.

Figures

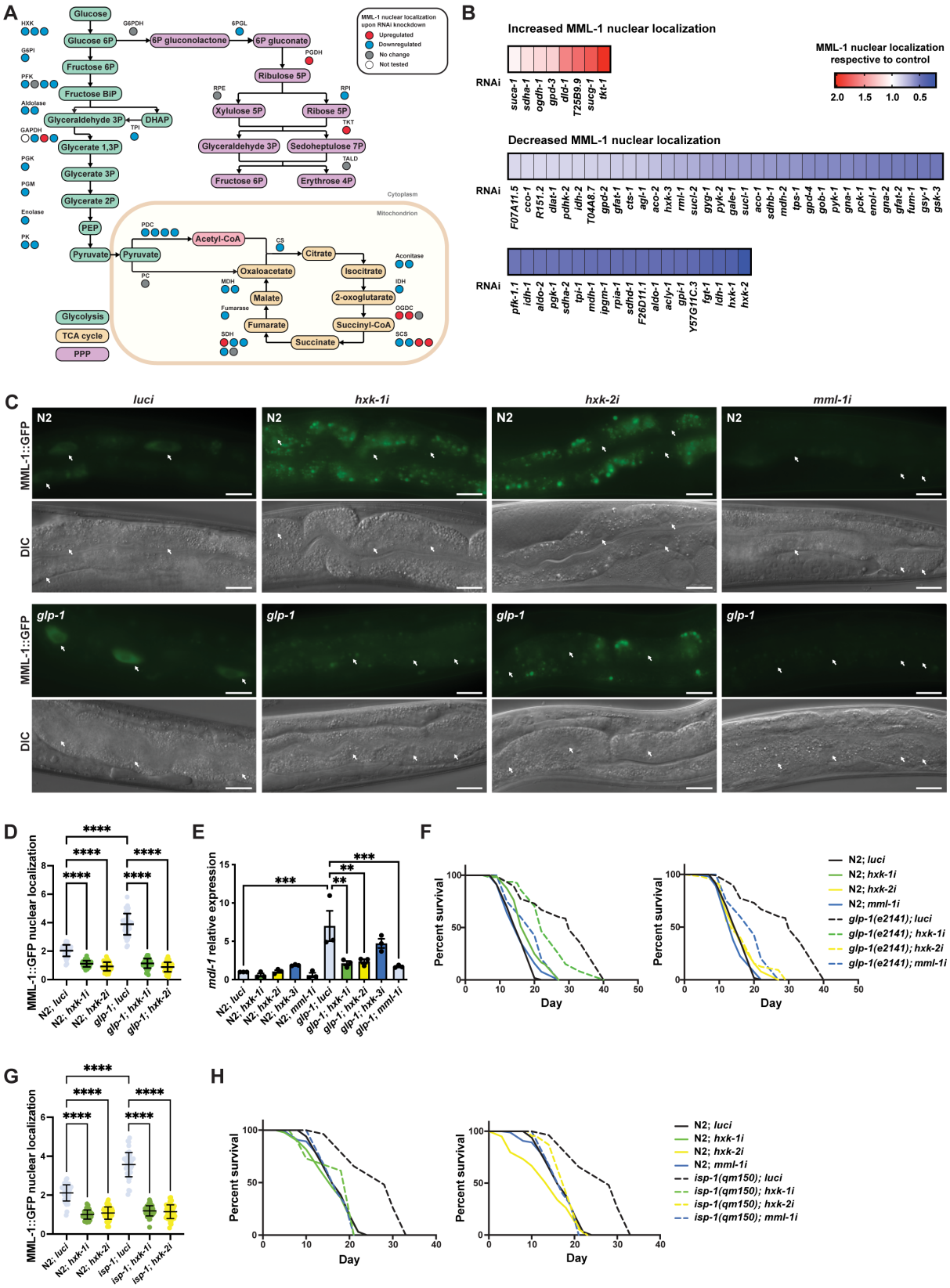

Figure 1. Hexokinases are required for germline longevity through the regulation of MML-1 localization and function. A. Screening for MML-1 regulators upon knockdown of glucose metabolism enzymes. For clarity, we only mapped the candidate genes involved in

886 glycolysis, TCA cycle, and PPP. See **Supplementary Table S1** for a complete list of genes
887 tested. MML-1::GFP (dhIs989) nuclear localization was measured in intestinal cells of day one
888 adult worms grown in the RNAi egg-on. Each circle represents one gene encoding an isozyme
889 or subunit of the complex. Circles are color-coded to indicate the increase (red) or decrease
890 (blue) of MML-1::GFP nuclear localization upon knockdown of the enzymes compared to
891 internal *luci* controls. DHAP, dihydroxyacetone phosphate; PEP, phosphoenolpyruvate; TCA
892 cycle, tricarboxylic acid cycle; PPP, pentose phosphate pathway. **B.** Quantification of MML-1
893 nuclear localization upon knockdown of glucose metabolism genes. Only genes that
894 statistically affected MML-1 nuclear localization compared to the internal *luci* control are
895 depicted ($p<0.05$; $N\geq2$). **C-D.** Representative images (**C**) and quantification (**D**) of MML-1
896 nuclear localization in wildtype and the germline-less *glp-1(e2141)* longevity background upon
897 knockdown of *luci* (control), *hxk-1i*, *hxk-2i*, and *mml-1i.* MML-1::GFP was quantified in nuclei
898 from intestinal cells (white arrows) in day one adult worms (N=3). Scale bars, 10 μm. **E.**
899 Relative mRNA levels of MML-1 downstream target *mdl-1* in young adult worms measured
900 by qPCR (N=3). **F.** Lifespans of wildtype and *glp-1(e2141)* upon *hxk-1* and *hxk-2* knockdown.
901 Lifespans for *hxk-1* and *hxk-2* knockdown were performed in the same experiment and plotted
902 separately for clarity; therefore, control lifespans are shared between plots. **G.** Quantification
903 of MML-1 nuclear localization in wildtype and *isp-1(qm150)* mutants upon *luci*, *hxk-1i*, and
904 *hxk-2i* in day one adult worms (N=3). **H.** Lifespan of wildtype and *isp-1(qm150)* upon *hxk-1*
905 and *hxk-2* knockdown (N=2). Statistical significance was calculated with *t*-test in **A** and **B,**
906 one-way ANOVA in **D** and **G**, two-tailed *t*-test in **E**, and Log-rank (Mantel-Cox) test in **F** and
907 **H**. **D** and **G** bars represent mean ± SD, and **E** bars represent mean ± SEM.
908

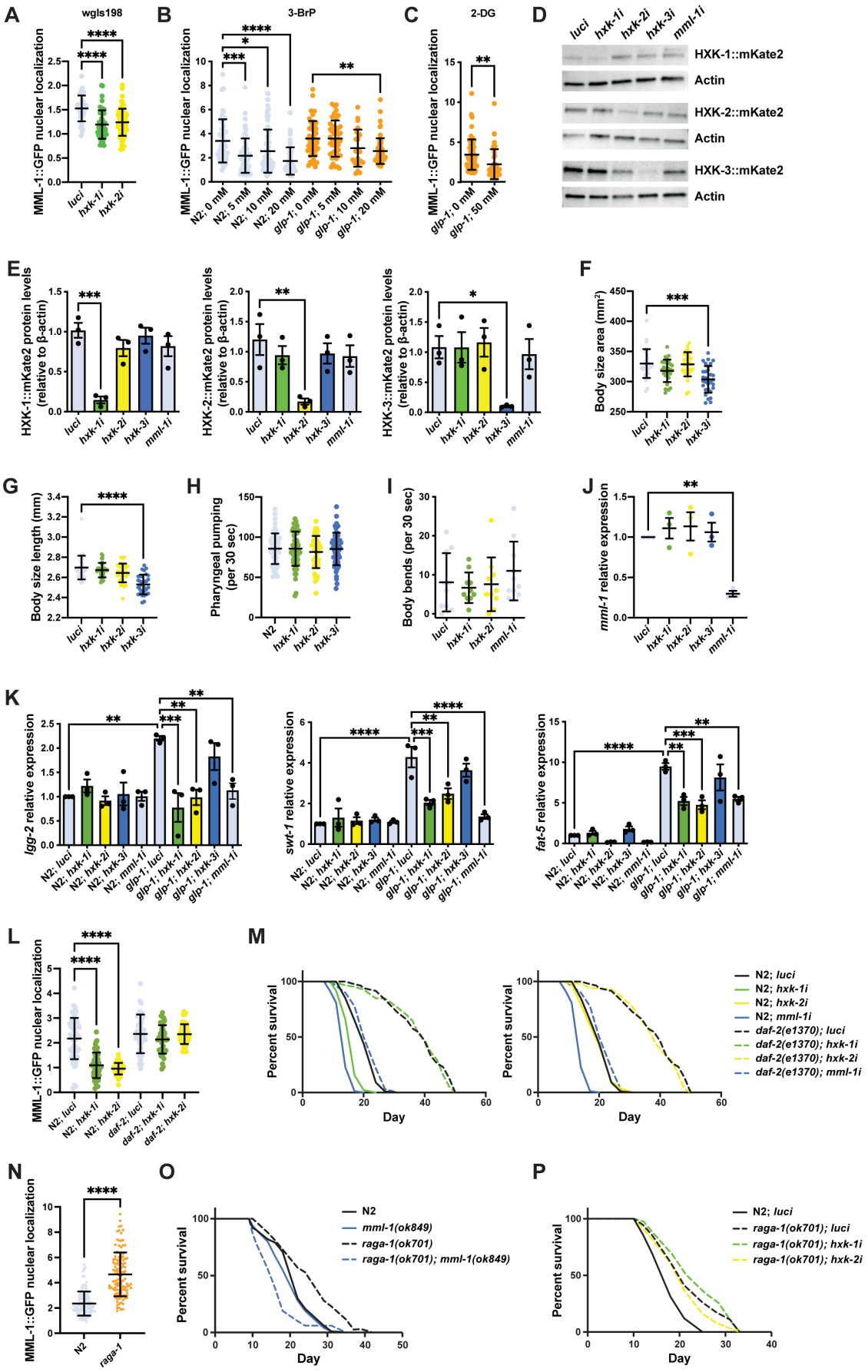
A
wgls198
MML-1::GFP nuclear localization
luci
hxk-1i
hxk-2i
B
3-BrP
MML-1::GFP nuclear localization
N2; 0 mM
N2; 5 mM
N2; 10 mM
N2; 20 mM
glp-1; 0 mM
glp-1; 5 mM
glp-1; 10 mM
glp-1; 20 mM
C
2-DG
MML-1::GFP nuclear localization
glp-1; 0 mM
glp-1; 50 mM
D
luci
hxk-1i
hxk-2i
hxk-3i
mml-1i
HXK-1::mKate2
Actin
HXK-2::mKate2
Actin
HXK-3::mKate2
Actin
E
HXK-1::mKate2 protein levels (relative to β-actin)
HXK-2::mKate2 protein levels (relative to β-actin)
HXK-3::mKate2 protein levels (relative to β-actin)
F
Body size area (mm²)
G
Body size length (mm)
H
Pharyngeal pumping (per 30 sec)
N2
I
Body bends (per 30 sec)
J
mml-1 relative expression
K
lgg-2 relative expression
swt-1 relative expression
fat-5 relative expression
N2; luci
N2; hxk-1i
N2; hxk-2i
N2; hxk-3i
N2; mml-1i
glp-1; luci
glp-1; hxk-1i
glp-1; hxk-2i
glp-1; hxk-3i
glp-1; mml-1i
L
MML-1::GFP nuclear localization
daf-2; luci
daf-2; hxk-1i
daf-2; hxk-2i
M
Percent survival
Day
N2; luci
N2; hxk-1i
N2; hxk-2i
N2; mml-1i
daf-2(e1370); luci
daf-2(e1370); hxk-1i
daf-2(e1370); hxk-2i
daf-2(e1370); mml-1i
N
MML-1::GFP nuclear localization
N2
raga-1
O
Percent survival
Day
N2
mml-1(ok849)
raga-1(ok701)
raga-1(ok701); mml-1(ok849)
P
Percent survival
Day
N2; luci
raga-1(ok701); luci
raga-1(ok701); hxk-1i
raga-1(ok701); hxk-2i

910 **Supplementary Figure 1. Hexokinases regulate MML-1 nuclear localization and**
911 **transcriptional function. A.** MML-1 nuclear localization in the fosmid line wgIs198 was
912 quantified in intestinal cells of day one adult worms using upon *hxk-1* and *hxk-2* knockdown
913 (N=3). **B**. Quantification of MML-1 nuclear localization in intestinal cells of day one adult
914 wildtype and *glp-1(e2141)* worms supplemented with the glycolytic inhibitor 3-bromopyruvate
915 (3-BrP) 5, 10, and 20 mM egg-on (N=2). **C**. Quantification of MML-1 nuclear localization in
916 intestinal cells of day one adult *glp-1(e2141)* worms supplemented with the glycolytic inhibitor
917 2-deoxy-glucose (2-DG) 50 mM egg-on (N=2). **D-E.** Representative Western blot (**D**) and
918 densitometry analysis (**E**) of hexokinases basal levels under *hxk-1i*, *hxk-2i*, *hxk-3i*, and *mml-1i*.
919 Protein levels were normalized to actin as a loading control (N=3). **F-H.** Measurements of body
920 size area (**F**), length (**G**), and pharyngeal pumping rate (**H**) of day one adult worms grown
921 under hexokinase knockdown (N=3). **I**. Motility assay of day one adult worms grown under
922 hexokinase knockdown (N=2). **J.** Relative *mml-1* mRNA levels under hexokinase knockdown
923 measured by qPCR (N=3). **K.** Relative mRNA expression of MML-1 downstream targets
924 *lgg-2*, *swt-1*, and *fat-5* measured by qPCR (N=3). **L.** Quantification of MML-1 nuclear
925 localization in wildtype and *daf-2(e1370)* mutants upon *luci*, *hxk-1i*, and *hxk-2i* in day one adult
926 worms (N=3). **M.** Lifespan of wildtype and *daf-2(e1370)* upon *hxk-1* and *hxk-2* knockdown
927 (N=2). **N.** Quantification of MML-1 nuclear localization in wildtype and *raga-1(ok701)*
928 mutants in day one adult worms (N=3). **O.** Lifespan of wildtype, *raga-1(ok701)*, *mml-1(ok849)*
929 and *raga-1 mml-1* double mutant (N=3). **P.** Lifespan of wildtype and *raga-1(ok701)* upon *hxk-1*
930 and *hxk-2* knockdown (N=3). Statistical significance was calculated with *t*-test in **C** and **N**,
931 one-way ANOVA in **A-B** and **E-L**, and Log-rank (Mantel-Cox) test in **M** and **O-P**. **A-C**, **F-J**,
932 **L**, and **N** bars represent mean **±** SD, and **E** and **K** bars represent mean **±** SEM.
933

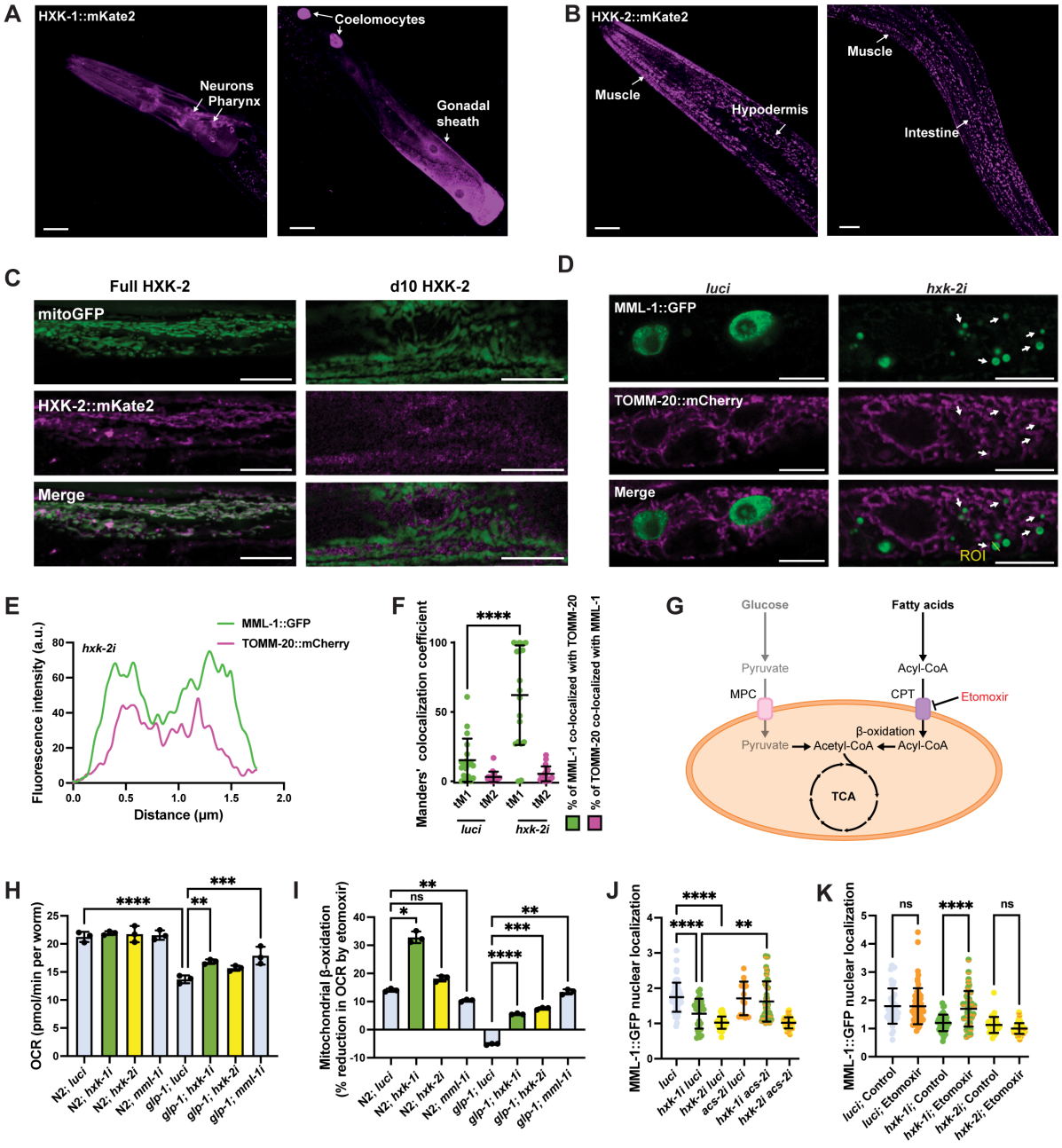

Figure 2. Enhanced mitochondrial β-oxidation suppresses MML-1 nuclear localization upon *hxk-1* knockdown. A-B. Tissue expression of HXK-1::mKate2 (**A**) and HXK-2::mKate2 (**B**) isozymes. The primary tissues are identified with arrows. Scale bars, 20 µm. **C.** Colocalization of mitochondrial reporter *myo-3p*::mitoGFP with full-length HXK-2::mKate2 and d10 HXK-2::mKate2 lacking the first ten residues of the N-terminus. Scale bars, 10 µm. **D.** Representative confocal images of day one adult worms expressing MML-1::GFP and the mitochondrial reporter *ges-1p*::TOMM-20::mCherry under *luci* and *hxk-2i*. Scale bars, 10 µm. **E.** Intensity plot of the region of interest (ROI) from *hxk-2i* (**D**). **F.** Colocalization of MML-1::GFP and TOMM-20::mCherry in *luci* and *hxk-2i*. The colocalization analysis was

945 calculated with the thresholded Mander's colocalization coefficients tM1 (GFP channel) and
946 tM2 (mCherry channel) (N=3). **G.** When glycolysis is reduced, cells rely on fatty acids for
947 energy production. Free fatty acids are activated to acyl-CoA and transported to the
948 mitochondria through the CPT in the mitochondrial outer membrane. The acyl-CoA is then
949 metabolized to generate acetyl-CoA that can enter the TCA cycle to produce energy. MPC,
950 mitochondrial pyruvate carrier; CPT, carnitine palmitoyltransferase. **H-I.** Oxygen consumption
951 rate (OCR) under basal conditions (**H**) and after the addition of the mitochondrial β-oxidation
952 inhibitor etomoxir (**I**). Mitochondrial β-oxidation is calculated as the percentage of decreased
953 OCR after the injection of etomoxir (N=3). **J.** MML-1 nuclear localization of day one adult
954 worms grown with double knockdown of *hxk-1* or *hxk-2* combined *acs-2i* (N=3). **K.** MML-1
955 nuclear localization of day one adult worms grown upon *hxk-1* and *hxk-2* knockdown with
956 supplementation of etomoxir 100 μM egg-on (N=3). Statistical significance was calculated
957 with *t*-test in **F**, and one-way ANOVA in **H-K**. **F** and **J-K** bars represent mean ± SD, **H-I** bars
958 represent mean ± SEM.
959

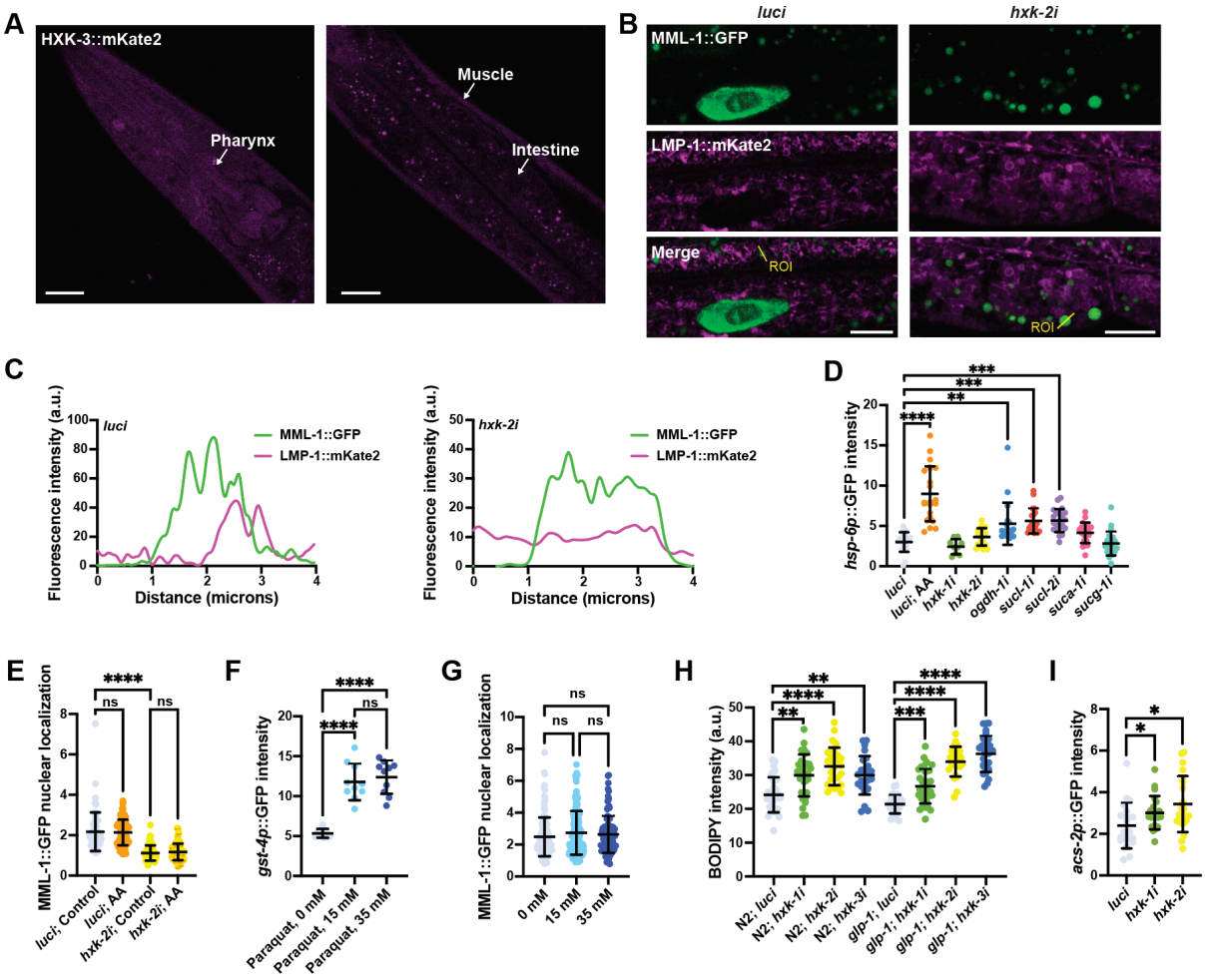

Supplementary Figure 2. MML-1 regulation by glucose metabolism is independent of mitochondrial and oxidative stress response. A. Localization of HXK-3::mKate2 isozyme. The primary tissues are identified with arrows. Scale bars, 20 µm. **B.** Representative confocal images of day one adult worms expressing MML-1::GFP and the lysosome/endosome reporter LMP-1::mKate2 under *luci* and *hxk-2i*. Scale bars, 10 µm. **C.** Intensity plots of the ROIs from **B** (n>10 MML-1 positive puncta per worm). **D.** Quantification of mitochondrial stress response *hsp-6p*::GFP transcriptional reporter upon knockdown of candidate genes regulating MML-1 nuclear localization. Worms were imaged on day one of adulthood. As a positive control for induction of mitochondrial stress, worms were supplemented with antimycin A (AA) 10 µg/mL for 24 h before imaging (N=3). **E.** Quantification of MML-1::GFP nuclear localization of worms grown under *luci* and *hxk-2i* supplemented with AA at the L4 stage, and nuclear localization was measured after 24 h (N=3). **F.** Quantification of day one adult worms expressing *gst-4p*::GFP transcriptional reporter exposed to paraquat for 6 h (N=3). **G.** Quantification of MML-1::GFP nuclear localization of day one adult worms exposed to

976 paraquat for 6 h (N=3). **H.** Neutral lipid content was measured on day one of adulthood by
977 feeding worms with C1-BODIPY-C12 egg-on (N=3). **I.** Quantification of day one adult worms
978 expressing the transcriptional reporter *acs-2p*::GFP under hexokinase knockdown (N=3).
979 Statistical significance was calculated with one-way ANOVA in **D-G**. **D-G** bars represent
980 mean ± SD.
981

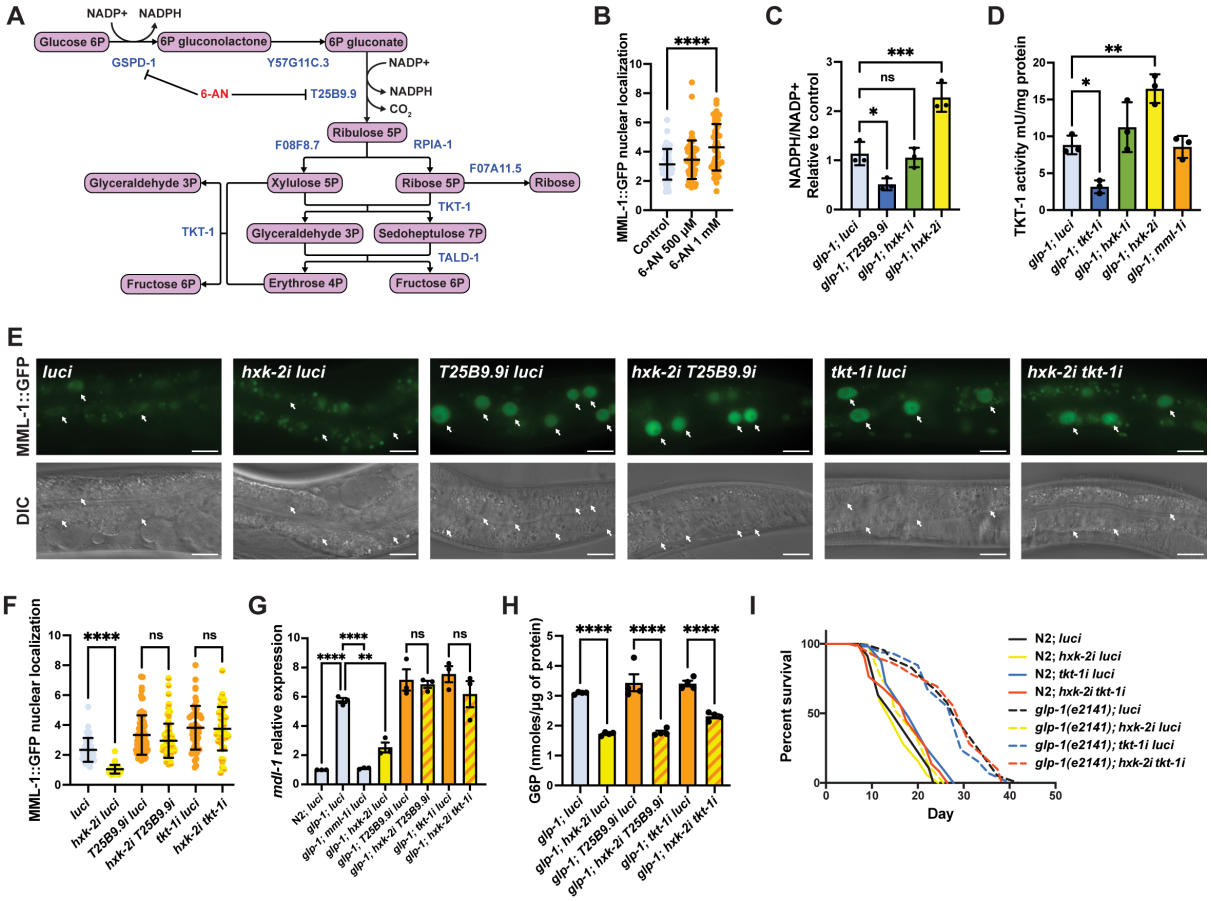

982
983 **Figure 3. HXK-2 regulates MML-1 localization and function through inhibition of the**
984 **PPP. A.** The PPP is a cytosolic pathway that metabolizes G6P to produce NADPH and ribose-
985 5P, and interconverts 3 to 7 carbon sugars. 6-Aminonicotinamide (6-AN) is a PPP inhibitor
986 that acts on the NADPH-producing enzymes GSPD-1 and T25B9.9. **B.** Quantification of
987 MML-1 nuclear localization of day one adult worms supplemented with 500 µM and 1 mM of
988 6-AN egg-on (N=3). **C.** Quantification of $NADP^+$ and NADPH levels in day one adult
989 *glp-1(e2141)* worms grown under hexokinase knockdown. *T25B9.9i* was used as a control.
990 Metabolite levels were normalized to total protein concentration (N=3). **D.** Transketolase
991 enzymatic activity assay in day one adult *glp-1(e2141)* worms grown under hexokinase
992 knockdown. *tkt-1i* was used as a control. Activity levels were normalized to total protein
993 concentration (N=3). **E-F.** Representative images (**E**) and quantification (**F**) of MML-1 nuclear

localization of day one adult worms upon double knockdown of *hxk-2* with the PPP enzymes *T25B9.9* and *tkt-1* (N=3). Scale bars, 20 µm. **G.** Relative mRNA levels of MML-1 downstream target *mdl-1* in young adult worms upon double knockdown of *hxk-2* in combination with enzymes of the PPP measured by qPCR (N=3). **H.** Quantification of G6P levels relative to total protein measured in day one adult *glp-1(e2141)* upon double knockdown of *hxk-2* in combination with enzymes of the PPP (N=4). **I.** Lifespan analysis of *glp-1(e2141)* with *hxk-2i* and *tkt-1i* single and double knockdowns. Lifespan was performed in the same experiment as **Supplementary Figure 3J**; therefore, control lifespans are shared between plots (N=3). Statistical significance was calculated with a one-way ANOVA test in **B-D** and **F-H**, and Log-rank (Mantel-Cox) test in **I**. **B** and **F** bars represent mean ± SD, **C-D** and **G-H** bars represent mean ± SEM.

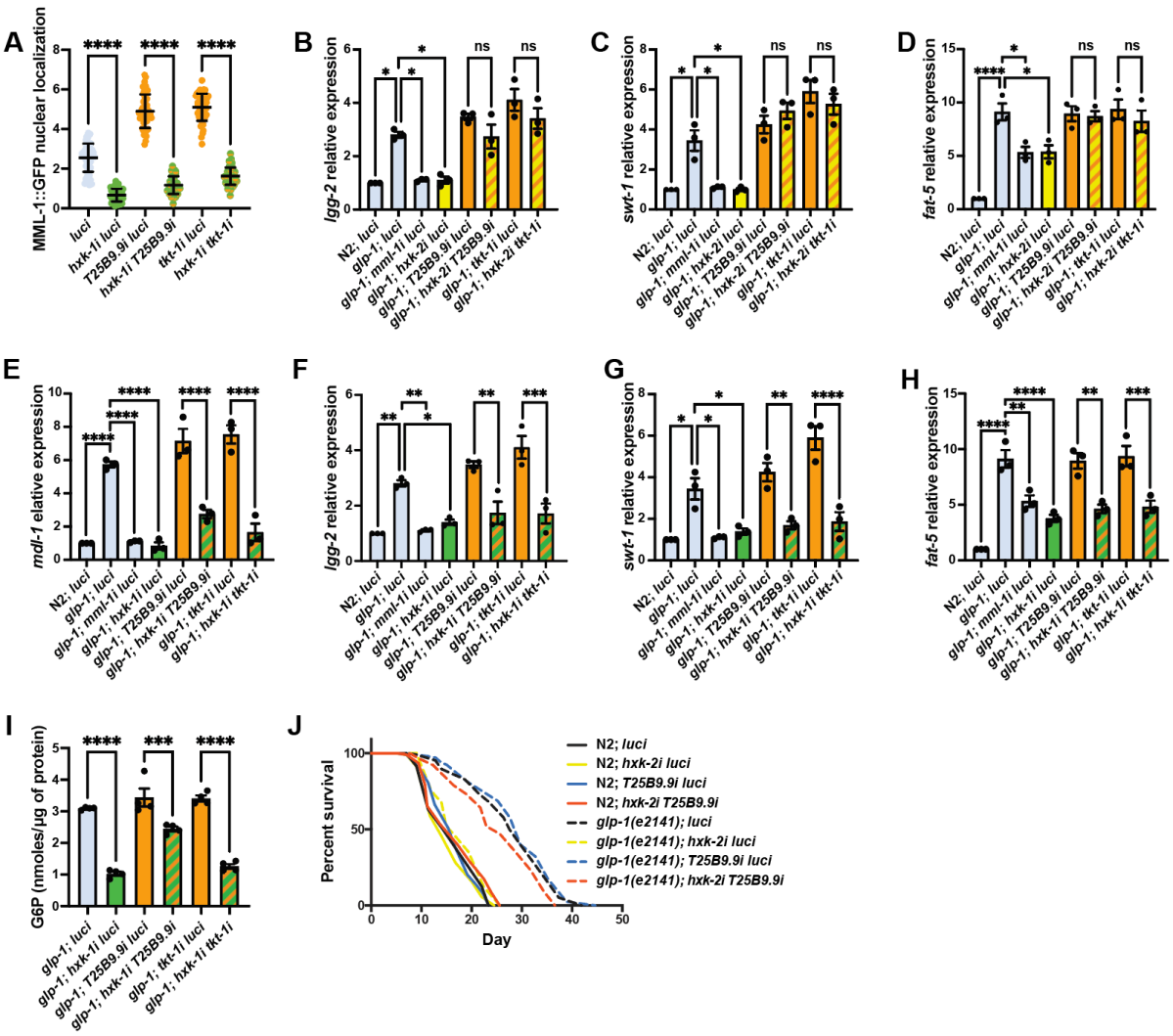

Supplementary Figure 3. HXK-1 and HXK-2 regulate MML-1 through parallel or independent pathways. A. MML-1 nuclear localization of day one adult worms upon double knockdown of *hxk-1* with enzymes of the PPP (N=3). **B-D.** Relative mRNA levels of MML-1 downstream targets *lgg-2* (**B**), *swt-1* (**C**), and *fat-5* (**D**) in young adult worms with double knockdown of *hxk-2* with enzymes of the PPP measured by qPCR (N=3). **E-H.** Relative mRNA levels of MML-1 downstream targets *mdl-1* (**E**), *lgg-2* (**F**), *swt-1* (**G**), and *fat-5* (**H**) in young adult worms with double knockdown of *hxk-1* with enzymes of the PPP measured by qPCR (N=3). **I**. Quantification of G6P levels relative to total protein measured in day one adult *glp-1(e2141)* worms grown under *hxk-1i* in combination with enzymes from the PPP (N=4). **J.** Lifespan analysis of *glp-1(e2141)* with *hxk-2i* and *T25B9.9i* single and double knockdowns. Lifespan was performed in the same experiment as **Figure 3I**; therefore, control lifespans are shared between plots (N=3). Statistical significance was calculated with a one-way ANOVA test in **A-I**, and Log-rank (Mantel-Cox) test in **J**. **A** bars represent mean ± SD, **B-I** bars represent mean ± SEM.

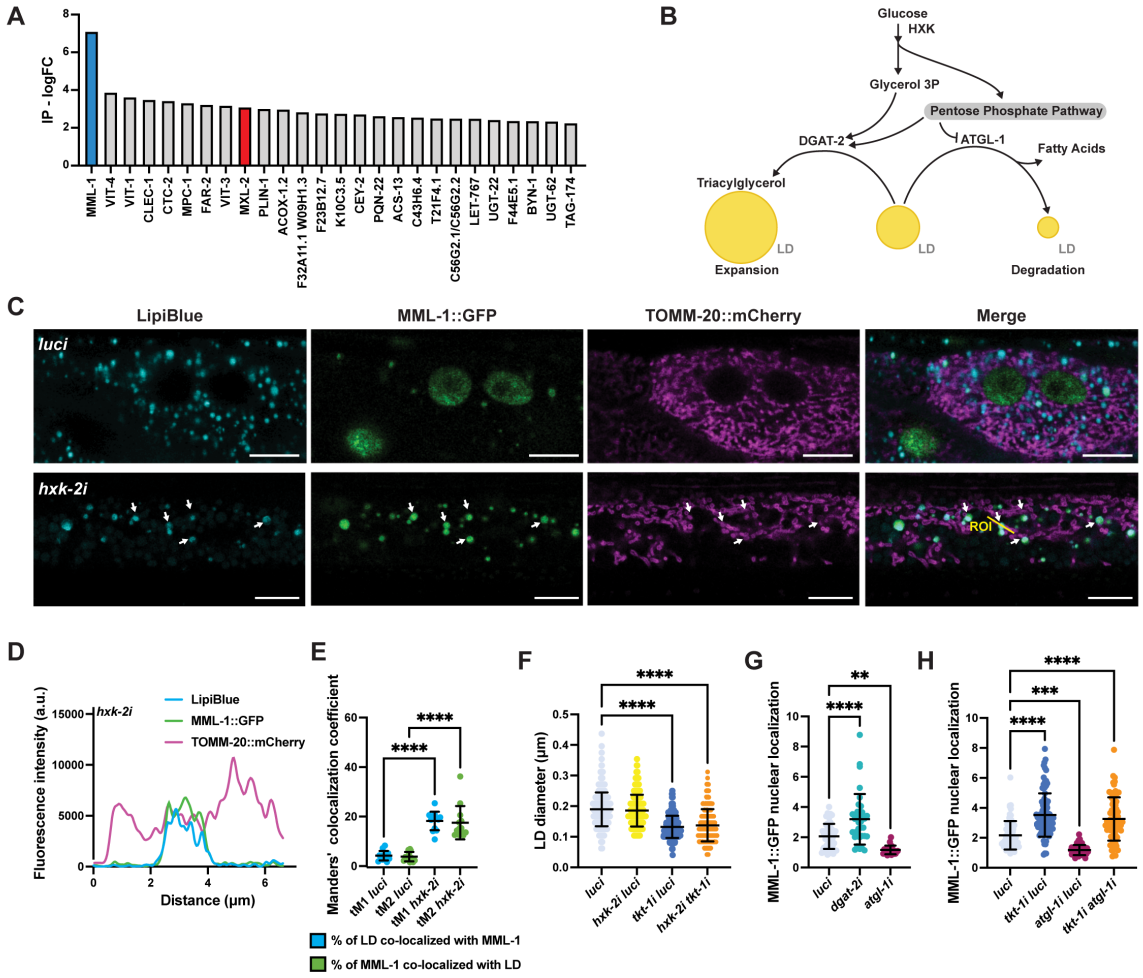

1024 **Figure 4. *hxk-2* knockdown increases MML-1 colocalization with LD. A.** Anti-FLAG
1025 immunoprecipitation (IP) from whole-worm lysates of animals expressing MML-1
1026 endogenously tagged with 3xFLAG in wildtype background. IP was analyzed by mass
1027 spectrometry (LC-MS/MS). The 25 top candidates co-enriched with MML-1 compared to non-
1028 transgenic wildtype control are shown as log FC, including MML-1 (blue) and its established
1029 binding partner MXL-2 (red). **B.** Crosstalk between glycolysis, PPP, and lipid droplet (LD)
1030 metabolism. On the one hand, LD expansion is favored by increased fatty acid synthesis and
1031 subsequent formation of triacylglycerol (TAG) by the diacylglycerol acetyltransferase
1032 DGAT-2. On the other hand, LD consumption releases free fatty acids from TAG by the rate-
1033 limiting lipase ATGL-1. **C.** Confocal microscopy of day one adult worms expressing
1034 MML-1::GFP and the mitochondrial reporter TOMM-20::mCherry stained with the LD dye
1035 LipiBlue under *luci* and *hxk-2i* (N=3). Scale bars, 10 μm. **D.** Intensity plot of the region of
1036 interest (ROI) from *hxk-2i* (**C**). **E.** Colocalization of MML-1::GFP and LD in *luci* and *hxk-2i*.
1037 The colocalization analysis was calculated with the thresholded Mander's colocalization
1038 coefficients tM1 (GFP channel) and tM2 (LipiBlue channel) (N=3). **F.** Quantification of LD
1039 diameter in day one adult worms expressing the LD reporter PLIN-1::mCherry upon
1040 knockdown of *hxk-2* and *tkt-1* (N=3). **G.** Quantification of MML-1 nuclear localization under
1041 knockdown of the LD metabolic enzymes *dgat-2* and *atg-1* (N=3). **H.** Quantification of
1042 MML-1 nuclear localization upon double knockdown of *tkt-1* and *atgl-1* (N=3). Statistical
1043 significance was calculated with a one-way ANOVA test in **E-H**. **E-H** bars represent mean ±
1044 SD.
1045

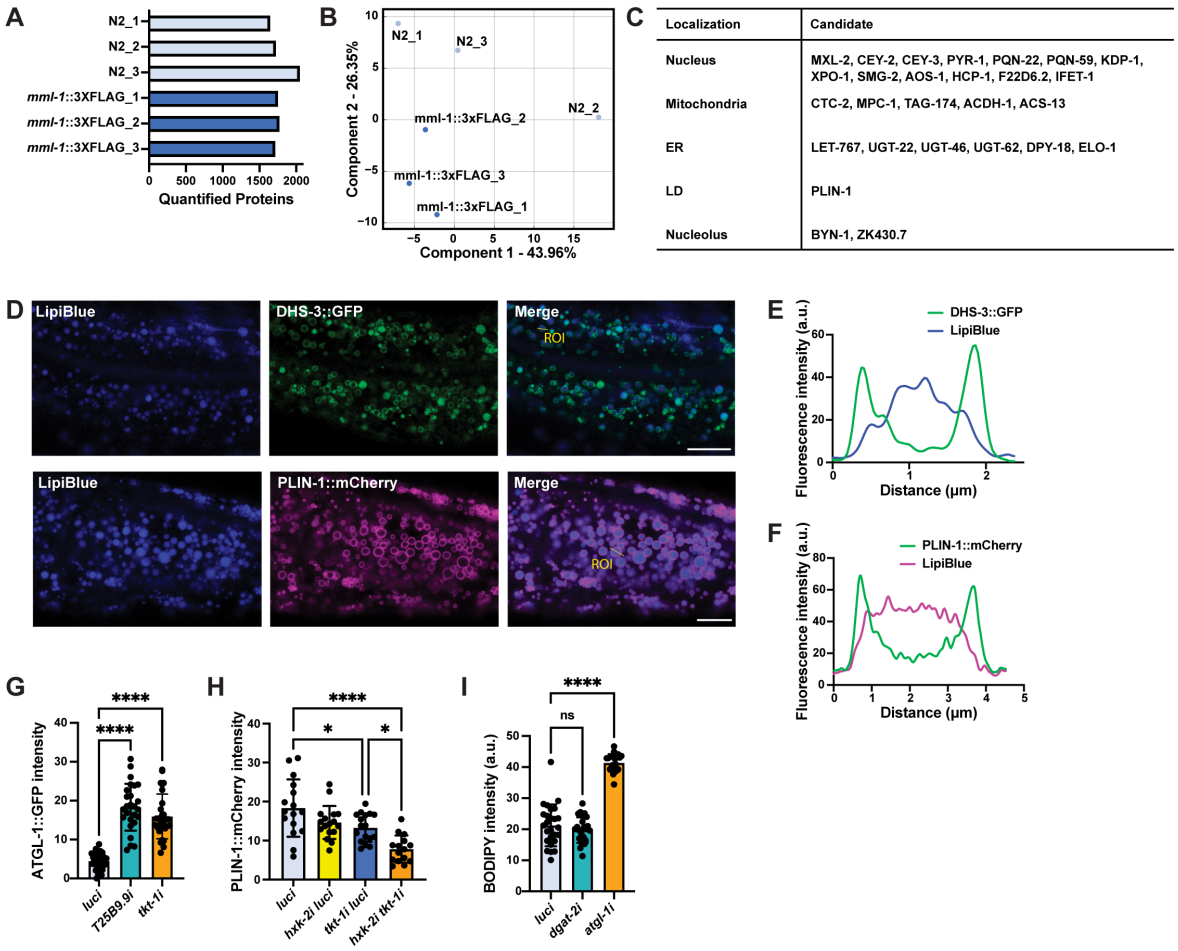

Supplementary Figure 4. MML-1 interactome is enriched with proteins from different organelles. A. Quantified proteins in each biological replicate of wildtype and *mml-1::3xFLAG* anti-FLAG immunoprecipitation (IP). **B**. Principal component analysis (PCA) with each biological replicate of the genotypes from proteomics. **C.** Top candidates co-enriched in MML-1::FLAG IP grouped by predicted subcellular localization (uniport.org). **D.** Representative images of day one adult worms expressing the LD proteins DHS-3::GFP and PLIN-1::mCherry reporters grown with the LD dye LipiBlue egg-on. Scale bars, 10 µm. **E-F.** Intensity plots of the marked ROI from **D** showing DHS-3::GFP (**E**) and PLIN-1::mCherry (**F**) colocalization with LipiBlue. **G.** Expression of the ATGL-1::GFP translational reporter measured on day one adult worms grown under *T25B9.9* and *tkt-1* RNAi egg-on (N=3). **H.** Quantification of LD reporter PLIN-1::mCherry intensity in day one adult worms upon knockdown of *hxk-2* and *tkt-1* (N=3). **I.** Quantification of neutral lipid content in day one adult worms supplemented with C1-BODIPY-C12 egg-on under *dgat-2* and *atgl-1* knockdown (N=3). Statistical significance was calculated with a one-way ANOVA test in **G-I**. **G-I** bars represent mean ± SD.

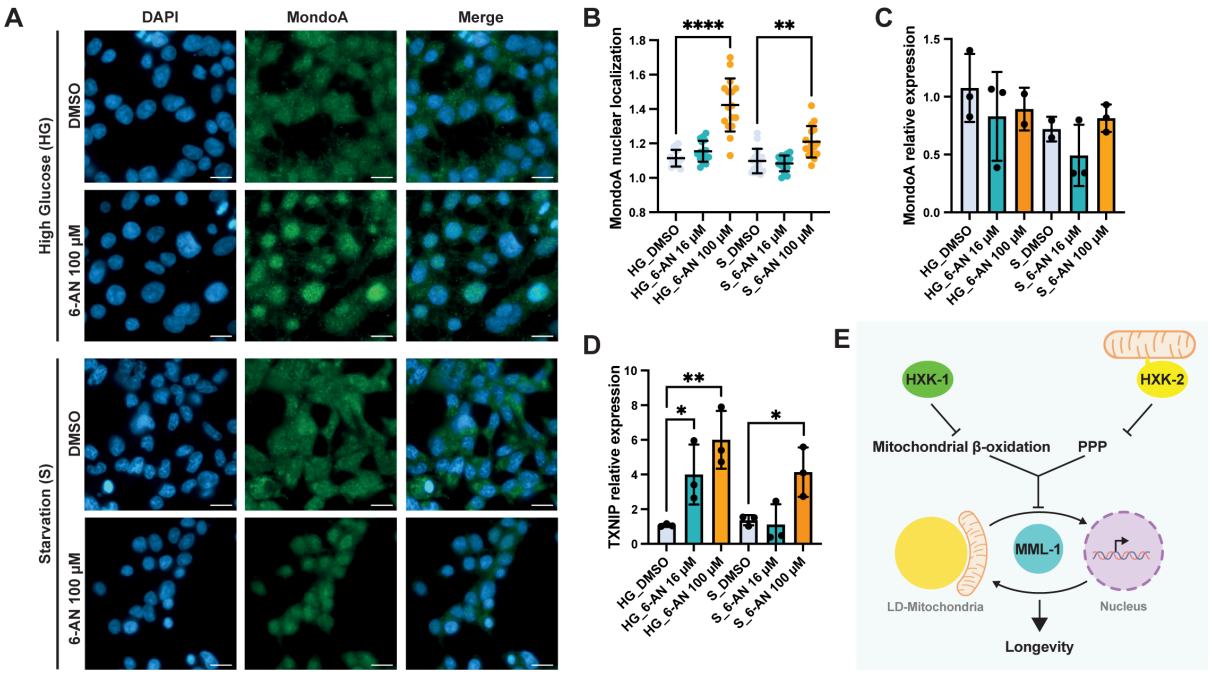

Figure 5. MondoA localization and transcriptional function is regulated by PPP in HEK293T cells. A. Immunofluorescence of MondoA in HEK293T cells under high glucose media (HG) and starvation (S) conditions supplemented with the PPP inhibitor 6-aminonicotinamide (6-AN) 100 μM. Scale bars, 20 μm. **B.** Quantification of MondoA nuclear localization in HEK293T cells treated with 6-AN 16 and 100 μM under HG and S conditions (N=3). **C.** Relative mRNA levels of *MondoA* in HEK293T cells treated with 6-AN 16 and 100 μM under HG and S conditions measured by qPCR (N=3). **D.** Relative mRNA levels of MondoA downstream target *TXNIP* in HEK293T cells treated with 6-AN 16 and 100 μM under HG and S conditions measured by qPCR (N=3). Statistical significance was calculated with one-way ANOVA in **B-D**. **B** bars represent mean ± SD, **C-D** bars represent mean ± SEM. **E.** Working model of MML-1 regulation by hexokinases. MML-1 is positively regulated by HXK-1 and HXK-2 through different downstream mechanisms. Inhibition of the mitochondrial β-oxidation rescues MML-1 nuclear localization upon *hxk-1i*, while decreasing enzymes from the PPP rescues MML-1 localization upon *hxk-2i*. These upstream mechanisms regulate MML-1 subcellular localization between LD-mitochondria and the nucleus, which is required for the lifespan extension mediated by germ-line loss. PPP, pentose phosphate pathway; LD, lipid droplet.

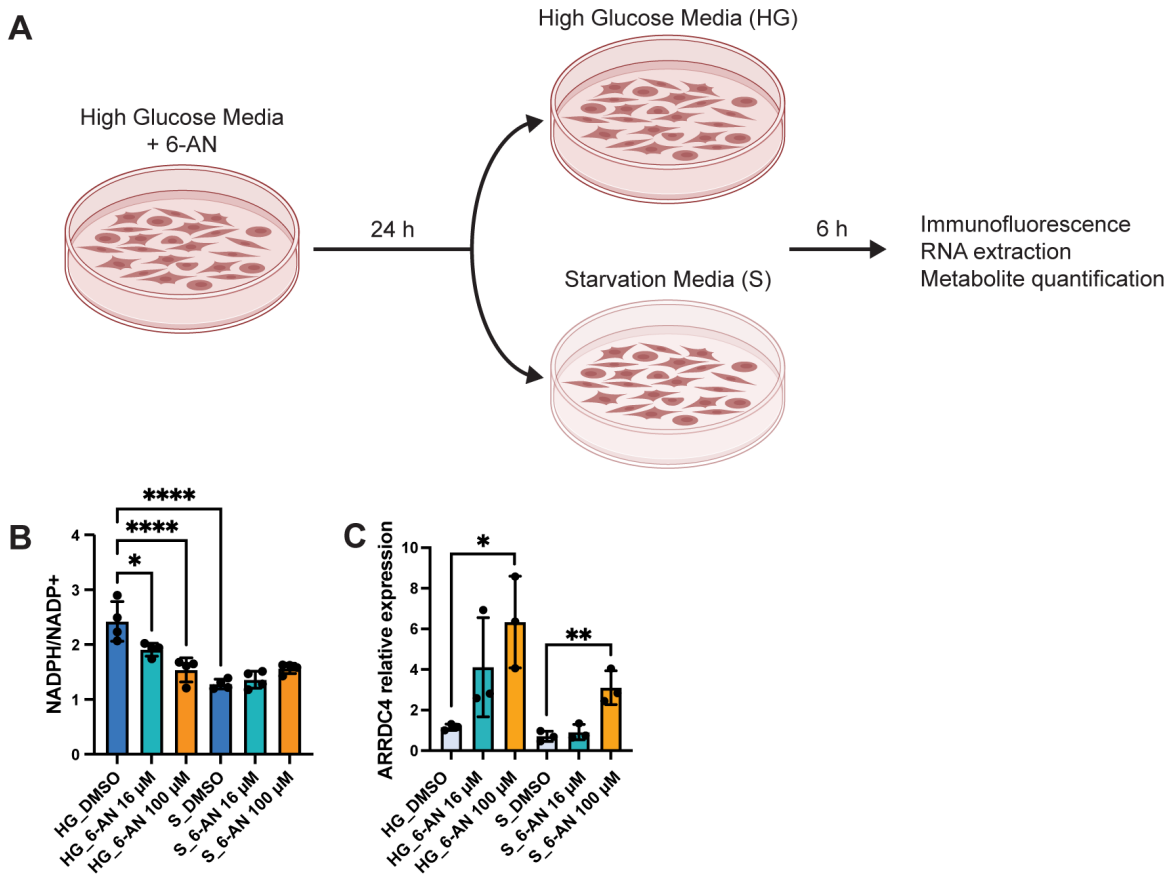

Supplementary Figure 5. Inhibition of PPP NADPH-producing enzymes by 6-AN induces MondoA downstream targets. A. Experimental design for inhibition of the PPP in HEK293T cells. Cells were grown in high glucose media (HG) supplemented with 6-AN for 24 h, and then the media was replaced with either HG or starvation (S) media for 6 h. Cells were collected and used for immunostaining, RNA extraction, and metabolite quantification. **B.** Quantification of $NADP^+$ and NADPH levels in HEK293T cells treated with 6-AN 16 and 100 µM under HG and S conditions (N=3). **C.** Relative mRNA levels of MondoA downstream target *ARRDC4* in HEK293T cells treated with 6-AN 16 and 100 µM under HG and S conditions measured by qPCR (N=3). Statistical significance was calculated with one-way ANOVA in **B-C**. **B-C** bars represent mean ± SEM.

References

Benhamed, F., Denechaud, P. D., Lemoine, M., Robichon, C., Moldes, M., Bertrand-Michel, J., Ratziu, V., Serfaty, L., Housset, C., Capeau, J., Girard, J., Guillou, H., & Postic, C. (2012). The lipogenic transcription factor ChREBP dissociates hepatic steatosis from insulin resistance in mice and humans. *Journal of Clinical Investigation*, *122*(6), 2176–2194. https://doi.org/10.1172/JCI41636

Bennett, C. F., Kwon, J. J., Chen, C., Russell, J., Acosta, K., Burnaevskiy, N., Crane, M. M., Bitto, A., Vander Wende, H., Simko, M., Pineda, V., Rossner, R., Wasko, B. M., Choi, H., Chen, S., Park, S., Jafari, G., Sands, B., Perez Olsen, C., … Kaeberlein, M. (2017). Transaldolase inhibition impairs mitochondrial respiration and induces a starvation-like longevity response in Caenorhabditis elegans. In *PLoS Genetics* (Vol. 13, Issue 3). https://doi.org/10.1371/journal.pgen.1006695

Billin, A. N., Eilers, A. L., Coulter, K. L., Logan, J. S., & Ayer, D. E. (2000). MondoA, a Novel Basic Helix-Loop-Helix–Leucine Zipper Transcriptional Activator That Constitutes a Positive Branch of a Max-Like Network. *Molecular and Cellular Biology*, *20*(23), 8845–8854. https://doi.org/10.1128/mcb.20.23.8845-8854.2000

Bolte, S., & Cordelières, F. P. (2006). A guided tour into subcellular colocalization analysis in light microscopy. *Journal of Microscopy*, *224*(3), 213–232. https://doi.org/10.1111/j.1365-2818.2006.01706.x

Boutant, M., Kulkarni, S. S., Joffraud, M., Ratajczak, J., Valera-Alberni, M., Combe, R., Zorzano, A., & Cantó, C. (2017). Mfn2 is critical for brown adipose tissue thermogenic function. *The EMBO Journal*, *36*(11), 1543–1558. https://doi.org/10.15252/embj.201694914

Bricker, D. K., Taylor, E. B., Schell, J. C., Orsak, T., Boutron, A., Chen, Y.-C., Cox, J. E., Cardon, C. M., Van Vranken, J. G., Dephoure, N., Redin, C., Boudina, S., Gygi, S. P., Brivet, M., Thummel, C. S., & Rutter, J. (2012). A Mitochondrial Pyruvate Carrier Required for Pyruvate Uptake in Yeast, Drosophila, and Humans. *Science*, *337*(July), 96–100. https://doi.org/10.1126/science.1218099

Carroll, P. A., Diolaiti, D., McFerrin, L., Gu, H., Djukovic, D., Du, J., Cheng, P. F., Anderson, S., Ulrich, M., Hurley, J. B., Raftery, D., Ayer, D. E., & Eisenman, R. N. (2015). Deregulated Myc Requires MondoA/Mlx for Metabolic Reprogramming and Tumorigenesis. *Cancer Cell*, *27*(2), 271–285. https://doi.org/10.1016/j.ccell.2014.11.024

Cha-Molstad, H., Saxena, G., Chen, J., & Shalev, A. (2009). Glucose-stimulated expression of Txnip is mediated by carbohydrate response element-binding protein, p300, and histone H4 acetylation in pancreatic beta cells. *Journal of Biological Chemistry*, *284*(25), 16898–16905. https://doi.org/10.1074/jbc.M109.010504

Chi, M. M. Y., Pusateri, M. E., Carter, J. G., Norris, B. J., McDougal, D. B., & Lowry, O. H. (1987). Enzymatic assays for 2-deoxyglucose and 2-deoxyglucose 6-phosphate. *Analytical Biochemistry*, *161*(2), 508–513. https://doi.org/10.1016/0003-2697(87)90481-7

1133 Chin, R. M., Fu, X., Pai, M. Y., Vergnes, L., Hwang, H., Deng, G., Diep, S., Lomenick, B.,
1134 Meli, V. S., Monsalve, G. C., Hu, E., Whelan, S. A., Wang, J. X., Jung, G., Solis, G. M.,
1135 Fazlollahi, F., Kaweeteerawat, C., Quach, A., Nili, M., … Huang, J. (2014). The
1136 metabolite α-ketoglutarate extends lifespan by inhibiting ATP synthase and TOR.
1137 *Nature*, *510*(7505), 397–401. https://doi.org/10.1038/nature13264
1138 Clancy, D. J., Gems, D., Harshman, L. G., Oldham, S., Stocker, H., Hafen, E., Leevers, S. J.,
1139 & Partridge, L. (2001). Extension of life-span by loss of CHICO, a Drosophila insulin
1140 receptor substrate protein. *Science*, *292*(5514), 104–106.
1141 https://doi.org/10.1126/science.1057991
1142 Cox, J., Hein, M. Y., Luber, C. A., Paron, I., Nagaraj, N., & Mann, M. (2014). Accurate
1143 proteome-wide label-free quantification by delayed normalization and maximal peptide
1144 ratio extraction, termed MaxLFQ. *Molecular and Cellular Proteomics*, *13*(9), 2513–
1145 2526. https://doi.org/10.1074/mcp.M113.031591
1146 Cox, J., & Mann, M. (2008). MaxQuant enables high peptide identification rates,
1147 individualized p.p.b.-range mass accuracies and proteome-wide protein quantification.
1148 *Nature Biotechnology*, *26*(12), 1367–1372. https://doi.org/10.1038/nbt.1511
1149 Dalziel, K., & Londesborough, J. C. (1968). The mechanisms of reductive carboxylation
1150 reactions: Carbon dioxide or bicarbonate as substrate of nicotinamide-adenine
1151 dinucleotide phosphate-linked isocitrate dehydrogenase and malic enzyme. *The*
1152 *Biochemical Journal*, *110*(2), 223–230. https://doi.org/10.1042/bj1100223
1153 Denechaud, P. D., Dentin, R., Girard, J., & Postic, C. (2008). Role of ChREBP in hepatic
1154 steatosis and insulin resistance. *FEBS Letters*, *582*(1), 68–73.
1155 https://doi.org/10.1016/j.febslet.2007.07.084
1156 Du, S., & Zheng, H. (2021). Role of FoxO transcription factors in aging and age-related
1157 metabolic and neurodegenerative diseases. *Cell and Bioscience*, *11*(1), 1–17.
1158 https://doi.org/10.1186/s13578-021-00700-7
1159 Fischer, F., Grigolon, G., Benner, C., & Ristow, M. (2022). Evolutionarily Conserved
1160 Transcription Factors As Regulators of Longevity and Targets for Geroprotection.
1161 *Physiological Reviews*, *102*(3), 1449–1494. https://doi.org/10.1152/physrev.00017.2021
1162 Gerisch, B., & Antebi, A. (2004). Hormonal signals produced by DAF-9/cytochrome P450
1163 regulate C. elegans dauer diapause in response to environmental cues. *Development*,
1164 *131*(8), 1765–1776. https://doi.org/10.1242/dev.01068
1165 Gerisch, B., Weitzel, C., Kober-Eisermann, C., Rottiers, V., & Antebi, A. (2001). A
1166 Hormonal Signaling Pathway Influencing C. elegans Metabolism, Reproductive

1167 Development, and Life Span. *Developmental Cell*, *1*(6), 841–851.
1168 https://doi.org/10.1016/S1534-5807(01)00085-5
1169 Ghasemi, A., Aghajani, H., Fallah, S., Assadi, M., & Seifi, M. (2015). C771G (His241Gln)
1170 polymorphism of MLXIPL Gene, TG levels and coronary artery disease: A case control
1171 study. *Anatolian Journal of Cardiology*, *15*(1), 8–12.
1172 https://doi.org/10.5152/akd.2014.5135
1173 Gordaliza-Alaguero, I., Cantó, C., & Zorzano, A. (2019). Metabolic implications of
1174 organelle–mitochondria communication. *EMBO Reports*, *20*(9), 1–27.
1175 https://doi.org/10.15252/embr.201947928
1176 Gottlob, K., Majewski, N., Kennedy, S., Kandel, E., Robey, R. B., & Hay, N. (2001).
1177 Inhibition of early apoptotic events by Akt/PKB is dependent on the first committed step
1178 of glycolysis and mitochondrial hexokinase. *Genes and Development*, *15*(11), 1406–
1179 1418. https://doi.org/10.1101/gad.889901
1180 Green, C. L., Lamming, D. W., & Fontana, L. (2021). Molecular mechanisms of dietary
1181 restriction promoting health and longevity. *Nature Reviews Molecular Cell Biology*,
1182 *0123456789*. https://doi.org/10.1038/s41580-021-00411-4
1183 Hutter, H., & Suh, J. (2016). GExplore 1.4: An expanded web interface for queries on
1184 Caenorhabditis elegans protein and gene function . *Worm*, *5*(4), e1234659.
1185 https://doi.org/10.1080/21624054.2016.1234659
1186 Iizuka, K., Miller, B., & Uyeda, K. (2006). Deficiency of carbohydrate-activated transcription
1187 factor ChREBP prevents obesity and improves plasma glucose control in leptin-deficient
1188 (ob/ob) mice. *American Journal of Physiology - Endocrinology and Metabolism*, *291*(2),
1189 358–364. https://doi.org/10.1152/ajpendo.00027.2006
1190 Ishii, S., Iizuka, K., Miller, B. C., & Uyeda, K. (2004). Carbohydrate response element
1191 binding protein directly promotes lipogenic enzyme gene transcription. *Proceedings of*
1192 *the National Academy of Sciences of the United States of America*, *101*(44), 15597–
1193 15602. https://doi.org/10.1073/pnas.0405238101
1194 John, S., Weiss, J. N., & Ribalet, B. (2011). Subcellular localization of hexokinases I and II
1195 directs the metabolic fate of glucose. *PLoS ONE*, *6*(3).
1196 https://doi.org/10.1371/journal.pone.0017674
1197 Johnson, D. W., Llop, J. R., Farrell, S. F., Yuan, J., Stolzenburg, L. R., & Samuelson, A. V.
1198 (2014). The Caenorhabditis elegans Myc-Mondo/Mad Complexes Integrate Diverse
1199 Longevity Signals. *PLoS Genetics*, *10*(4). https://doi.org/10.1371/journal.pgen.1004278
1200 Ju, H. Q., Lin, J. F., Tian, T., Xie, D., & Xu, R. H. (2020). NADPH homeostasis in cancer:

1201 functions, mechanisms and therapeutic implications. *Signal Transduction and Targeted*
1202 *Therapy*, *5*(1), 1–12. https://doi.org/10.1038/s41392-020-00326-0
1203 Kaadige, M. R., Looper, R. E., Kamalanaadhan, S., & Ayer, D. E. (2009). Glutamine-
1204 dependent anapleurosis dictates glucose uptake and cell growth by regulating MondoA
1205 transcriptional activity. *Proceedings of the National Academy of Sciences of the United*
1206 *States of America*, *106*(35), 14878–14883. https://doi.org/10.1073/pnas.0901221106
1207 Kamath, R. S., & Ahringer, J. (2003). Genome-wide RNAi screening in Caenorhabditis
1208 elegans. *Methods*, *30*(4), 313–321. https://doi.org/10.1016/S1046-2023(03)00050-1
1209 Kennedy, B. K., & Lamming, D. W. (2016). The Mechanistic Target of Rapamycin: The
1210 Grand ConducTOR of Metabolism and Aging. *Cell Metabolism*, *23*(6), 990–1003.
1211 https://doi.org/10.1016/j.cmet.2016.05.009
1212 Koopman, M., Michels, H., Dancy, B. M., Kamble, R., Mouchiroud, L., Auwerx, J., Nollen,
1213 E. A. A., & Houtkooper, R. H. (2016). A screening-based platform for the assessment of
1214 cellular respiration in Caenorhabditis elegans. *Nature Protocols*, *11*(10), 1798–1816.
1215 https://doi.org/10.1038/nprot.2016.106
1216 Krahmer, N., Najafi, B., Schueder, F., Quagliarini, F., Steger, M., Seitz, S., Kasper, R.,
1217 Salinas, F., Cox, J., Uhlenhaut, N. H., Walther, T. C., Jungmann, R., Zeigerer, A.,
1218 Borner, G. H. H., & Mann, M. (2018). Organellar Proteomics and Phospho-Proteomics
1219 Reveal Subcellular Reorganization in Diet-Induced Hepatic Steatosis. *Developmental*
1220 *Cell*, *47*(2), 205-221.e7. https://doi.org/10.1016/j.devcel.2018.09.017
1221 Lapierre, L. R., De Magalhaes Filho, C. D., McQuary, P. R., Chu, C. C., Visvikis, O., Chang,
1222 J. T., Gelino, S., Ong, B., Davis, A. E., Irazoqui, J. E., Dillin, A., & Hansen, M. (2013).
1223 The TFEB orthologue HLH-30 regulates autophagy and modulates longevity in
1224 Caenorhabditis elegans. *Nature Communications*, *4*.
1225 https://doi.org/10.1038/ncomms3267
1226 Lee, S.-J., Murphy, C.T., & Kenyon, C. (2009). Glucose Shortens the Lifespan of
1227 *Caenorhabditis elegans* by Down-Regulating Aquaporin Gene Expression. *Cell*
1228 *Metabolism, 10*(5), 379-391. https://doi.org/10.1016/j.cmet.2009.10.003
1229 Lee, J. H., Kong, J., Jang, J. Y., Han, J. S., Ji, Y., Lee, J., & Kim, J. B. (2014). Lipid Droplet
1230 Protein LID-1 Mediates ATGL-1-Dependent Lipolysis during Fasting in Caenorhabditis
1231 elegans. *Molecular and Cellular Biology*, *34*(22), 4165–4176.
1232 https://doi.org/10.1128/mcb.00722-14
1233 Leigh-Brown, S., Enriquez, J. A., & Odom, D. T. (2010). Nuclear transcription factors in
1234 mammalian mitochondria. *Genome Biology*, *11*(7), 1–9. https://doi.org/10.1186/gb-

1235 2010-11-7-215
1236 Li, F., Wang, Y., Zeller, K. I., Potter, J. J., Wonsey, D. R., O'Donnell, K. A., Kim, J.,
1237 Yustein, J. T., Lee, L. A., & Dang, C. V. (2005). Myc Stimulates Nuclearly Encoded
1238 Mitochondrial Genes and Mitochondrial Biogenesis. *Molecular and Cellular Biology*,
1239 *25*(14), 6225–6234. https://doi.org/10.1128/mcb.25.14.6225-6234.2005
1240 Lindén, M., Gellerfors, P., & Dean Nelson, B. (1982). Pore protein and the hexokinase-
1241 binding protein from the outer membrane of rat liver mitochondria are identical. *FEBS*
1242 *Letters*, *141*(2), 189–192. https://doi.org/10.1016/0014-5793(82)80044-6
1243 Ma, L., Robinson, L. N., & Towle, H. C. (2006). ChREBP·Mlx is the principal mediator of
1244 glucose-induced gene expression in the liver. *Journal of Biological Chemistry*, *281*(39),
1245 28721–28730. https://doi.org/10.1074/jbc.M601576200
1246 Marchenko, N. D., Wolff, S., Erster, S., Becker, K., & Moll, U. M. (2007).
1247 Monoubiquitylation promotes mitochondrial p53 translocation. *EMBO Journal*, *26*(4),
1248 923–934. https://doi.org/10.1038/sj.emboj.7601560
1249 Marinov, G. K., Wang, Y. E., Chan, D., & Wold, B. J. (2014). Evidence for site-specific
1250 occupancy of the mitochondrial genome by nuclear transcription factors. *PLoS ONE*,
1251 *9*(1), 1–24. https://doi.org/10.1371/journal.pone.0084713
1252 Massari, M. E., & Murre, C. (2000). *Helix-Loop-Helix Proteins: Regulators of Transcription*
1253 *in Eucaryotic*. *20*(2), 429–440. https://doi.org/10.1128/mcb.20.2.429-440.2000
1254 Mejhert, N., Kuruvilla, L., Gabriel, K. R., Elliott, S. D., Guie, M. A., Wang, H., Lai, Z. W.,
1255 Lane, E. A., Christiano, R., Danial, N. N., Farese, R. V., & Walther, T. C. (2020).
1256 Partitioning of MLX-Family Transcription Factors to Lipid Droplets Regulates
1257 Metabolic Gene Expression. *Molecular Cell*, *77*(6), 1251-1264.e9.
1258 https://doi.org/10.1016/j.molcel.2020.01.014
1259 Motola, D. L., Cummins, C. L., Rottiers, V., Sharma, K. K., Li, T., Li, Y., Suino-Powell, K.,
1260 Xu, H. E., Auchus, R. J., Antebi, A., & Mangelsdorf, D. J. (2006). Identification of
1261 Ligands for DAF-12 that Govern Dauer Formation and Reproduction in C. elegans. *Cell*,
1262 *124*(6), 1209–1223. https://doi.org/10.1016/j.cell.2006.01.037
1263 Mutlu, A. S., Gao, S. M., Zhang, H., & Wang, M. C. (2020). Olfactory specificity regulates
1264 lipid metabolism through neuroendocrine signaling in Caenorhabditis elegans. *Nature*
1265 *Communications*, *11*(1), 1–15. https://doi.org/10.1038/s41467-020-15296-8
1266 Nakamura, S., Karalay, Ö., Jäger, P. S., Horikawa, M., Klein, C., Nakamura, K., Latza, C.,
1267 Templer, S. E., Dieterich, C., & Antebi, A. (2016). Mondo complexes regulate TFEB
1268 via TOR inhibition to promote longevity in response to gonadal signals. *Nature*

Communications, *7*. https://doi.org/10.1038/ncomms10944

Orlandi, I., Coppola, D. P., & Vai, M. (2014). Rewiring yeast acetate metabolism through mpc1 loss of function leads to mitochondrial damage and decreases chronological lifespan. *Microbial Cell*, *1*(12), 393–405. https://doi.org/10.15698/mic2014.12.178

Owen, O. E., Kalhan, S. C., & Hanson, R. W. (2002). The key role of anaplerosis and cataplerosis for citric acid cycle function. *Journal of Biological Chemistry*, *277*(34), 30409–30412. https://doi.org/10.1074/jbc.R200006200

Papsdorf, K., Miklas, J. W., Hosseini, A., Cabruja, M., Morrow, C. S., Savini, M., Yu, Y., Silva-garcía, C. G., Haseley, N. R., Murphy, L. M., Yao, P., Launoit, E. De, Dixon, S. J., Snyder, M. P., Wang, M. C., Mair, W. B., & Brunet, A. (2023). Lipid droplets and peroxisomes are co-regulated to drive lifespan extension in response to mono-unsaturated fatty acids. *Nature Cell Biology*. https://doi.org/10.1038/s41556-023-01136-6

Pastorino, J. G., Shulga, N., & Hoek, J. B. (2002). Mitochondrial binding of hexokinase II inhibits Bax-induced cytochrome c release and apoptosis. *Journal of Biological Chemistry*, *277*(9), 7610–7618. https://doi.org/10.1074/jbc.M109950200

Penkov, S., Kaptan, D., Erkut, C., Sarov, M., Mende, F., & Kurzchalia, T. V. (2015). Integration of carbohydrate metabolism and redox state controls dauer larva formation in Caenorhabditis elegans. *Nature Communications*, *6*. https://doi.org/10.1038/ncomms9060

Pickett, C. L., Breen, K. T., & Ayer, D. E. (2007). A C. elegans Myc-like network cooperates with semaphorin and Wnt signaling pathways to control cell migration. *Developmental Biology*, *310*(2), 226–239. https://doi.org/10.1016/j.ydbio.2007.07.034

Postic, C., Dentin, R., Denechaud, P. D., & Girard, J. (2007). ChREBP, a transcriptional regulator of glucose and lipid metabolism. *Annual Review of Nutrition*, *27*, 179–192. https://doi.org/10.1146/annurev.nutr.27.061406.093618

R Core Team. (2017). *R: A language and environment for statistical computing* (3.4.3). R Foundation for Statistical Computing. https://www.r-project.org/

Ralser, M., Wamelink, M. M., Struys, E. A., Joppich, C., Krobitsch, S., Jakobs, C., & Lehrach, H. (2008). A catabolic block does not sufficiently explain how 2-deoxy-D-glucose inhibits cell growth. *Proceedings of the National Academy of Sciences of the United States of America*, *105*(46), 17807–17811. https://doi.org/10.1073/pnas.0803090105

Ramachandran, P. V., Savini, M., Folick, A. K., Hu, K., Masand, R., Graham, B. H., &

Wang, M. C. (2019). Lysosomal Signaling Promotes Longevity by Adjusting Mitochondrial Activity. *Developmental Cell*, *48*(5), 685-696.e5. https://doi.org/10.1016/j.devcel.2018.12.022

Rambold, A. S., Cohen, S., & Lippincott-Schwartz, J. (2015). Fatty acid trafficking in starved cells: Regulation by lipid droplet lipolysis, autophagy, and mitochondrial fusion dynamics. *Developmental Cell*, *32*(6), 678–692. https://doi.org/10.1016/j.devcel.2015.01.029

Richards, P., Ourabah, S., Montagne, J., Burnol, A. F., Postic, C., & Guilmeau, S. (2017). MondoA/ChREBP: The usual suspects of transcriptional glucose sensing; Implication in pathophysiology. *Metabolism: Clinical and Experimental*, *70*, 133–151. https://doi.org/10.1016/j.metabol.2017.01.033

Ritchie, M. E., Phipson, B., Wu, D., Hu, Y., Law, C. W., Shi, W., & Smyth, G. K. (2015). limma powers differential expression analyses for RNA-sequencing and microarray studies. *Nucleic Acids Research*, *43*(7), e47. https://doi.org/10.1093/nar/gkv007

Roberts, D. J., Tan-Sah, V. P., Ding, E. Y., Smith, J. M., & Miyamoto, S. (2014). Hexokinase-II Positively Regulates Glucose Starvation-Induced Autophagy through TORC1 Inhibition. *Molecular Cell*, *53*(4), 521–533. https://doi.org/10.1016/j.molcel.2013.12.019

Rual, J. F., Ceron, J., Koreth, J., Hao, T., Nicot, A. S., Hirozane-Kishikawa, T., Vandenhaute, J., Orkin, S. H., Hill, D. E., van den Heuvel, S., & Vidal, M. (2004). Toward improving Caenorhabditis elegans phenome mapping with an ORFeome-based RNAi library. *Genome Research*, *14*(10 B), 2162–2168. https://doi.org/10.1101/gr.2505604

Sans, C. L., Satterwhite, D. J., Stoltzman, C. A., Breen, K. T., & Ayer, D. E. (2006). MondoA-Mlx Heterodimers Are Candidate Sensors of Cellular Energy Status: Mitochondrial Localization and Direct Regulation of Glycolysis. *Molecular and Cellular Biology*, *26*(13), 4863–4871. https://doi.org/10.1128/mcb.00657-05

Schulz, T.J., Zarse, K., Voigt, A., Urban, N., Birringer, M., & Ristow, M. (2007). Glucose Restriction Extends *Caenorhabditis elegans* Life Span by Inducing Mitochondrial Respiration and Increasing Oxidative Stress. *Cell Metabolism*, *6*(4), 280-293. https://doi.org/10.1016/j.cmet.2007.08.011

Selman, C., Lingard, S., Choudhury, A. I., Batterham, R. L., Claret, M., Clements, M., Ramadani, F., Okkenhaug, K., Schuster, E., Blanc, E., Piper, M. D., Al-Qassab, H., Speakman, J. R., Carmignac, D., Robinson, I. C. A., Thornton, J. M., Gems, D., Partridge, L., & Withers, D. J. (2008). Evidence for lifespan extension and delayed age–

1337 related biomarkers in insulin receptor substrate 1 null mice. *The FASEB Journal*, *22*(3),
1338 807–818. https://doi.org/10.1096/fj.07-9261com
1339 Stoltzman, C. A., Kaadige, M. R., Peterson, C. W., & Ayer, D. E. (2011). MondoA senses
1340 non-glucose sugars: Regulation of thioredoxin-interacting protein (TXNIP) and the
1341 hexose transport curb. *Journal of Biological Chemistry*, *286*(44), 38027–38034.
1342 https://doi.org/10.1074/jbc.M111.275503
1343 Stoltzman, C. A., Peterson, C. W., Breen, K. T., Muoio, D. M., Billin, A. N., & Ayer, D. E.
1344 (2008). Glucose sensing by MondoA:Mlx complexes: A role for hexokinases and direct
1345 regulation of thioredoxin-interacting protein expression. *Proceedings of the National*
1346 *Academy of Sciences of the United States of America*, *105*(19), 6912–6917.
1347 https://doi.org/10.1073/pnas.0712199105
1348 Sui, D., & Wilson, J. E. (1997). Structural determinants for the intracellular localization of
1349 the isozymes of mammalian hexokinase: Intracellular localization of fusion constructs
1350 incorporating structural elements from the hexokinase isozymes and the green
1351 fluorescent protein. *Archives of Biochemistry and Biophysics*, *345*(1), 111–125.
1352 https://doi.org/10.1006/abbi.1997.0241
1353 Tatenaka, Y., Kato, H., Ishiyama, M., Sasamoto, K., Shiga, M., Nishitoh, H., & Ueno, Y.
1354 (2019). Monitoring Lipid Droplet Dynamics in Living Cells by Using Fluorescent
1355 Probes. *Biochemistry*, *58*(6), 499–503. https://doi.org/10.1021/acs.biochem.8b01071
1356 Tong, X., Zhao, F., Mancuso, A., Gruber, J. J., & Thompson, C. B. (2009). The glucose-
1357 responsive transcription factor ChREBP contributes to glucose-dependent anabolic
1358 synthesis and cell proliferation. *Proceedings of the National Academy of Sciences of the*
1359 *United States of America*, *106*(51), 21660–21665.
1360 https://doi.org/10.1073/pnas.0911316106
1361 Van Gilst, M. R., Hadjivassiliou, H., & Yamamoto, K. R. (2005). A Caenorhabditis elegans
1362 nutrient response system partially dependent on nuclear receptor NHR-49. *Proceedings*
1363 *of the National Academy of Sciences of the United States of America*, *102*(38), 13496–
1364 13501. https://doi.org/10.1073/pnas.0506234102
1365 Vrablik, T. L., Petyuk, V. A., Larson, E. M., Smith, R. D., & Watts, J. L. (2015). Lipidomic
1366 and proteomic analysis of Caenorhabditis elegans lipid droplets and identification of
1367 ACS-4 as a lipid droplet-associated protein. *Biochimica et Biophysica Acta - Molecular*
1368 *and Cell Biology of Lipids*, *1851*(10), 1337–1345.
1369 https://doi.org/10.1016/j.bbalip.2015.06.004
1370 Wang, M. C., O'Rourke, E. J., & Ruvkun, G. (2008). Fat metabolism links germline stem

cells and longevity in C. elegans. *Science*, *322*(5903), 957–960. https://doi.org/10.1126/science.1162011

Wilde, B. R., Ye, Z., Lim, T. Y., & Ayer, D. E. (2019). Cellular acidosis triggers human mondoa transcriptional activity by driving mitochondrial atp production. *ELife*, *8*, 1–25. https://doi.org/10.7554/eLife.40199

Wilson, J. E. (2003). Isozymes of mammalian hexokinase: Structure, subcellular localization and metabolic function. *Journal of Experimental Biology*, *206*(12), 2049–2057. https://doi.org/10.1242/jeb.00241

Wolf, A. J., Reyes, C. N., Liang, W., Becker, C., Shimada, K., Wheeler, M. L., Cho, H. C., Popescu, N. I., Coggeshall, K. M., Arditi, M., & Underhill, D. M. (2016). Hexokinase Is an Innate Immune Receptor for the Detection of Bacterial Peptidoglycan. *Cell*, *166*(3), 624–636. https://doi.org/10.1016/j.cell.2016.05.076

Yamamoto-Imoto, H., Minami, S., Shioda, T., Yamashita, Y., Sakai, S., Maeda, S., Yamamoto, T., Oki, S., Takashima, M., Yamamuro, T., Yanagawa, K., Edahiro, R., Iwatani, M., So, M., Tokumura, A., Abe, T., Imamura, R., Nonomura, N., Okada, Y., … Yoshimori, T. (2022). Age-associated decline of MondoA drives cellular senescence through impaired autophagy and mitochondrial homeostasis. *Cell Reports*, *38*(9), 110444. https://doi.org/10.1016/j.celrep.2022.110444

Yamashita, H., Takenoshita, M., Sakurai, M., Bruick, R. K., Henzel, W. J., Shillinglaw, W., Arnot, D., & Uyeda, K. (2001). A glucose-responsive transcription factor that regulates carbohydrate metabolism in the liver. *Proceedings of the National Academy of Sciences of the United States of America*, *98*(16), 9116–9121. https://doi.org/10.1073/pnas.161284298

Yamawaki, T. M., Berman, J. R., Suchanek-Kavipurapu, M., McCormick, M., Gaglia, M. M., Lee, S. J., & Kenyon, C. (2010). The somatic reproductive tissues of C. elegans promote longevity through steroid hormone signaling. *PLoS Biology*, *8*(8), 45–46. https://doi.org/10.1371/journal.pbio.1000468

Zhang, Y., Lanjuin, A., Chowdhury, S. R., Mistry, M., Silva-García, C. G., Weir, H. J., Chia-Lin, L., Escoubas, C. C., Tabakovic, E., & Mair, W. B. (2019). Neuronal TORC1 modulates longevity via ampk and cell nonautonomous regulation of mitochondrial dynamics in C. Elegans. *ELife*, *8*, 1–24. https://doi.org/10.7554/eLife.49158